THE UNIVERSITY of EDINBURGH

Edinburgh Research Explorer

Improved forest height estimation by fusion of simulated GEDI Lidar data and TanDEM-X InSAR data

OPEN ACCESS

1 **Improved forest height estimation by fusion of simulated GEDI Lidar data and**

2 **TanDEM-X InSAR data**

3 Wenlu Qi [a], Seung-Kuk Lee [b], Steven Hancock [a], Scott Luthcke [b], Hao Tang [a], John Armston [a],

4 Ralph Dubayah [a]

5 [a] Department of Geographical Sciences, University of Maryland, College Park, MD, USA

6 [b] NASA Goddard Space Flight Center, Greenbelt, MD, USA

7 **ABSTRACT**

8   Interferometric Synthetic Aperture Radar (InSAR) and lidar are increasingly used active remote

9 sensing techniques for forest structure observation. The TanDEM-X (TDX) InSAR mission of

10 German Aerospace Center (DLR) and the upcoming Global Ecosystem Dynamics Investigation

11 (GEDI) of National Aeronautics and Space Administration (NASA) together may provide more

12 accurate estimates of global forest structure and biomass via their synergic use. In this paper, we

13 explored the efficacy of simulated GEDI data in improving height estimates from TDX InSAR

14 data. Our study sites span three major forest types: a temperate forest, a mountainous conifer forest,

15 and a tropical rainforest. The GEDI lidar coverage was simulated for the full nominal two-year

16 mission duration, under both cloud-free and 50%-cloud conditions. We then used these GEDI data

17 to parameterize the Random Volume over Ground (RVoG) model driven by TDX imagery. In

18 particular, we explored the following three strategies for forest structure estimation: 1) TDX data

19 alone; 2) TDX + GEDI-derived digital terrain model (DTM); and 3) TDX + GEDI DTM + GEDI

20 canopy height. We then validated the retrieved forest heights against wall-to-wall airborne lidar

21 measurements. We found relatively large biases at 90 [m] spatial resolution, from 4.2 – 11.9 [m],

22 and root mean square errors (RMSEs), from 7.9 – 12.7 [m] when using TDX data alone under

23 constrained RVoG assumptions of a fixed extinction coefficient (σ) and a zero ground-to-volume

24 amplitude ratio ($\mu=0$). Results improved significantly with the aid of a DTM derived from GEDI

25 data which enabled estimation of spatially-varying σ values (vs. fixed extinction) under a $\mu=0$

26 assumption, with biases reduced to 1.7 – 4.2 [m] and RMSEs to 4.9 – 8.6 [m] across cloudy and

27 cloud-free cases. The best agreement was achieved in the third strategy by also incorporating

28 information of GEDI-derived canopy height to further enhance the RVoG parameters. The

29 improved model, when still assuming $\mu = 0$, reduced biases to less than or close to one meter and

30 further reduced RMSEs to 4.0 – 6.7 [m]. Finally, we used GEDI data to estimate spatially-varying

31 μ in the RVoG model. We found biases of between -0.7 – 0.9 [m] and RMSEs in the range from

32 2.6 – 7.1 [m] over the three sites. Our results suggest that use of GEDI data improves height

33 inversion from TDX, providing heights at more accuracy than can be achieved by TDX alone, and

34 enabling wall-to-wall height estimation at much finer spatial resolution than can be achieved by

35 GEDI alone.

36 **Keywords:**

38 **1   Introduction**

39 Forest Above-Ground Biomass (AGB) has been identified as a key parameter for assessing the

40 role of forests in the global carbon cycle and for analyzing ecosystem productivity. However,

41 current quantification of forest AGB worldwide and associated biomass changes remain uncertain

42 (CEOS 2014; Pan et al. 2011). Forest inventory methods have been widely used to estimate AGB

43 at field scales, either through destructive sampling or by measurement of various biomass-related

44   forest structural properties and a subsequent employment of allometric equations. However, these

45   methods are often labor-intensive and time-consuming, and do not yield continuous AGB maps

46   over the landscape (Clark and Kellner 2012; Duncanson et al. 2015a; Duncanson et al. 2015b;

47   Keller et al. 2001). Therefore, there is an interest to capitalize on field-scale biomass and remotely

48   measured forest parameters (particularly height) to provide more cost-effective AGB mappings at

49   large areas (Goetz and Dubayah 2011; Huang et al. 2012).

50   Lidar and Interferometric Synthetic Aperture Radar (InSAR) remote sensing techniques are

51   playing increasingly important roles in estimating important forest structural attributes (Goetz and

52   Dubayah 2011; Hajnsek et al. 2009; Hall et al. 2011). These attributes have been related to field-

53   based biomass estimates for mapping forest AGB over the landscape using both parametric

54   (Nelson et al. 2017; Solberg et al. 2013) and non-parametric modeling techniques (Blackard et al.

55   2008; Kellndorfer et al. 2012). However, taken individually, each technique has particular

56   limitations and difficulties to deliver large-area forest structure dataset for reducing the uncertainty

57   of forest AGB quantification (Goetz and Dubayah 2011; Hall et al. 2011). Lidar-based biomass

58   estimates are mainly restricted to local regions where airborne lidar campaigns were conducted

59   (Drake et al. 2003; Huang et al. 2012; Swatantran et al. 2011). Data from the sole spaceborne Earth

60   observation lidar instrument, Geoscience Laser Altimeter System (GLAS) onboard Ice, Cloud, and

61   land Elevation Satellite (ICESat), have been used to produce consistent forest structure AGB maps

62   at the continental or global scales by integrating with other spaceborne remote sensing data, such

63   as radar and multispectral observations. However, unless aggregated to coarse resolutions (often

64   larger than a few kilometers) these estimates were often associated with large uncertainties,

65   primarily due to the low sensitivity of the used ancillary data to the full range of forest vertical

66   structure and biomass, and the low sampling density of GLAS, particularly over mid-latitude and

67   tropical forests (Baccini et al. 2012; Hu et al. 2016; Nelson et al. 2017; Saatchi et al. 2011).

68   InSAR has been widely used to generate wall-to-wall forest structure and biomass maps (Lei

69   and Siqueira 2015; Schlund et al. 2015; Soja et al. 2014). However, accuracies of InSAR products

70   are often reduced by temporal decorrelation which occurs when the SAR images forming the

71   interferometric coherence are acquired at different times. This temporal decorrelation limits the

72   accuracy of repeat-pass interferometry (Lavalle and Hensley 2015; Lee et al. 2013; Papathanassiou

73   and Cloude 2003). To address this problem, the German Aerospace Center (DLR) launched the

74   first dual-satellite (bistatic) SAR spaceborne mission – TanDEM-X (TDX). There is no temporal

75   decorrelation using TDX because the data from each satellite are obtained at the same time,

76   allowing more accurate estimation of forest height and biomass (Askne et al. 2013; Kugler et al.

77   2014; Persson et al. 2017; Treuhaft et al. 2015). A simple forest scattering model, the Random

78   Volume over Ground (RVoG) model, has been widely used to produce forest height maps from

79   TDX coherence under a variety of terrain conditions and forest types. However, because TDX

80   images are generally acquired at a single polarization, determination of forest height using the

81   RVoG model must assume known canopy extinction and topographic parameters (Hajnsek et al.

82   2009; Kugler et al. 2014; Qi and Dubayah 2016).

83   The aforementioned issues of lidar and InSAR potentially may be addressed by combining their

84   complementary observations, where lidar data are used to constrain the forest scattering model and

85   to validate InSAR height inversion while InSAR images are exploited to extend lidar observations

86   (Bergen et al. 2009; Goetz and Dubayah 2011; Hall et al. 2011; Qi and Dubayah 2016; Sun et al.

87   2011). For example, previous studies have used airborne lidar elevation data to provide the needed

88   external DTM to estimate forest height from TDX single-polarization (single-pol) coherence

89 (Cloude et al. 2013; Kugler et al. 2014; Schlund et al. 2015; Soja and Ulander 2013; Solberg et al.

90 2013). Accurate airborne lidar observations of forest vertical structure have also been used to

91 enhance parameterization of the forest scattering models for improved forest height estimation

92 (Brolly et al. 2016). The elevation data derived from the first spaceborne InSAR mission – Shuttle

93 Radar Topography Mission (SRTM) – has been calibrated and validated with local height

94 measurements from GLAS to produce continuous canopy height and AGB maps over Mangrove

95 forests (Fatoyinbo and Simard 2013). These studies have demonstrated the potential advantages in

96 combining lidar and InSAR to map forest structure at better accuracy and coverage.

97   An unprecedented opportunity of global forest structure and biomass mapping from

98 lidar/InSAR fusion has emerged with the upcoming launch of the Global Ecosystem Dynamics

99 Investigation (GEDI) mission (Qi and Dubayah 2016). GEDI is a full-waveform lidar system to

100 be deployed on the International Space Station (ISS) by NASA in 2018 (Stysley et al. 2015).

101 During its nominal two-year mission, GEDI will provide about 15 billion ground elevation and

102 forest vertical structure measurements at a footprint size of ~25 m in diameter. Aided by these

103 GEDI observations, TDX data can potentially provide wall-to-wall forest height maps, which in

104 turn can be used to extend GEDI observations for forest structure and biomass estimation at finer

105 resolution, accuracy and coverage (Qi and Dubayah 2016). However, the effects of using different

106 elements of forest vertical structure observed by GEDI on TDX height inversion are still unclear

107 and largely unexplored. Also, the performance of GEDI/TDX fusion needs to be investigated for

108 different forest structural types and environmental conditions.

109   The goal of this paper is to develop lidar/InSAR fusion methods for improved TDX height

110 estimates using GEDI observations. GEDI data are simulated using airborne laser scanning (ALS)

111 data and combined with single-pol TDX InSAR data. Our test sites include three contrasting forest

112   types: Hubbard Brook Experimental Forest (HBEF), a temperate mixed broadleaf deciduous and

113   conifer forest; Teakettle Experimental Forest (TEF), a mountainous conifer forest; and La Selva

114   Biological Station (LSBS), a tropical broadleaf rainforest. Specifically we perform three sets of

115   analyses to explore the impact on height derivations using fusion. First, we establish a baseline

116   accuracy for our study sties by using only TDX data and simple assumptions of RVoG parameters.

117   Next, we utilize an external DTM derived from simulated GEDI data in the RVoG model. Lastly,

118   we investigate the impact of using both a simulated GEDI DTM and GEDI-derived canopy heights

119   within the RVoG model. In each case, we also examine the impact of clouds and phenology on the

120   fusion results by comparison of GEDI tracks under cloud-free vs. 50%-cloud conditions, and

121   comparison of leaf-on vs. leaf-off TDX acquisitions. Results from this study should help inform

122   potential approaches towards improved mapping of forest height and biomass using lidar and

123   InSAR remote sensing.

2   Test Sites and Data
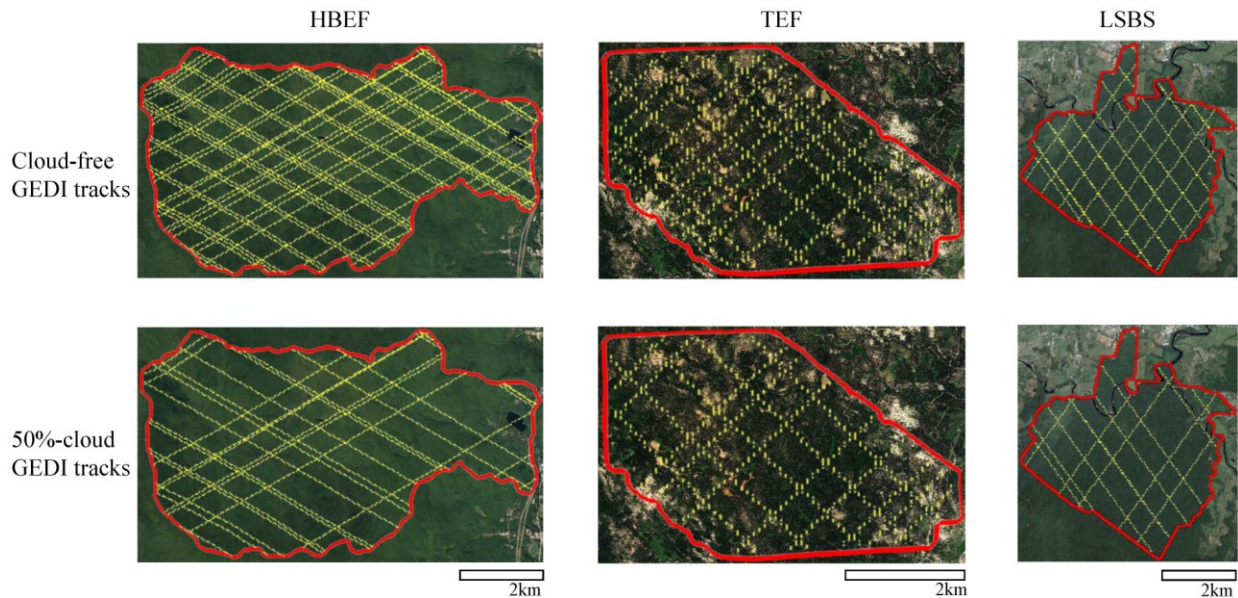
2.1   Test sites

Fig. 1 Simulated two-year GEDI tracks over HBEF, TEF and LSBS test sites respectively based on cloud-free and 50%-cloud cover conditions.

Three sites were chosen, representing a range of forest characteristics (Fig. 1). Hubbard Brook Experimental Forest (HBEF) (43°56′12″N, 71°45′01″W) is a closed-canopy broadleaf-dominated forest located in the White Mountain National Forest, New Hampshire, USA, and is typical of temperate forest conditions. Covering an area of 3,100 ha the topography of the site is rugged, with steep slopes occurring within a bowl-shaped watershed. Elevations range from about 150 m to 1000 m. It is a managed forest consisting of mostly deciduous northern hardwoods and a small percentage (10–20%) of spruce-fir. Measured forest heights mainly range from ~2 to ~42 m, with a mean of ~24 m and a standard deviation of ~5 m. HBEF has a moderate amount of above ground

137   biomass, with a mean of 216 Mg/ha in 2001 (Qi and Dubayah 2016; Schwarz et al. 2001; Siccama

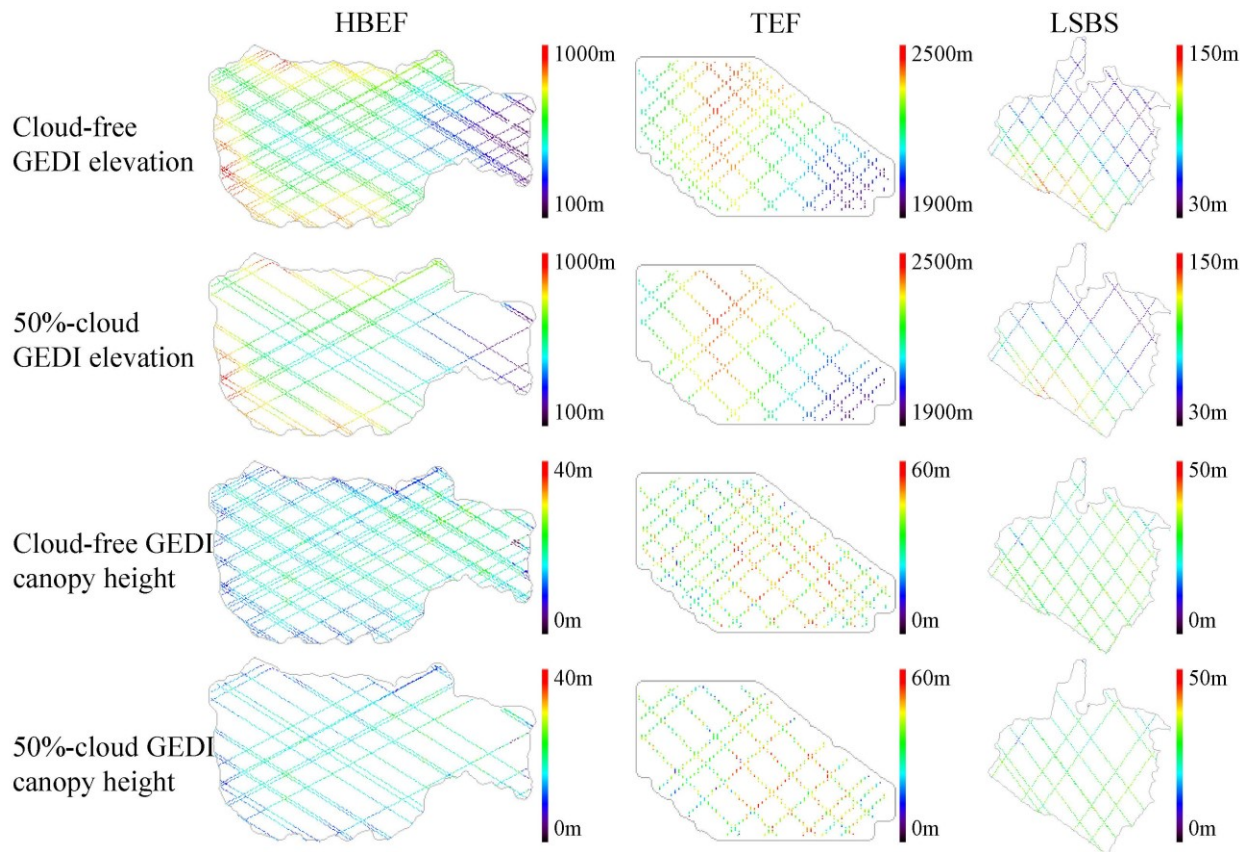138   et al. 2007; Whitehurst et al. 2013).

139   Teakettle Experimental Forest (TEF) (36°57′60″N, 119°01′0″W) is a conifer-dominated forest

140   located along the western slopes of Sierra Nevada Mountain Range, USA. The study site is a

141   mountainous region covering an area of around 1,300 ha, with elevations ranging from about 1,800

142   m to 2,500 m elevation. It is an old-growth forest with mature and complex structure. Tree heights

143   mainly range from ~3 m to ~68 m, with a mean height of ~39 m and a standard deviation of ~11

144   m. Major tree types include White fir (*Abies concolor*), Ponderosa pine (*Pinus ponderosa*), Red

145   fir (*Abies magnifica*) and California black oak (*Quercus kellogi*) (Pierce et al. 2002). The averaged

146   aboveground biomass is about 200 Mg/ha with individual tree values up to 20 Mg per tree

147   (Duncanson et al. 2015a; Smith et al. 2005; Swatantran et al. 2011).

148   La Selva Biological Station (LSBS) (10°25′44″N, 84°00′29″W) is a low-land (elevation <150

149   m) tropical rain forest in northeastern Costa Rica. The site is a protected region covering about

150   1,600 ha, and contains a mixture of old-growth, secondary and selectively logged forests as well

151   as agroforestry plantations, developed areas, and abandoned pastures. Tree height ranges from ~3

152   to ~59 m, with a mean of ~28 m and a standard deviation of ~11 m. Estimate of aboveground

153   biomass spans from 0 to 279 Mg/ha, and averaged biomass of old-growth forest, which is the major

154   components of total LSBS biomass, is around 169 Mg/ha (Clark et al. 2011). Detailed site

155   characteristics can be found in (Clark et al. 2008; Dubayah et al. 2010; Tang et al. 2014; Tang et

156   al. 2012).

2.2 Datasets

2.2.1 Airborne lidar data

Small-footprint discrete return lidar data were collected over HBEF in September 2009 when trees were in leaf-on condition. An Optech ALTM 3100 instrument collected data with an average point density of 4.0 shots per square meter, and up to four returns for each laser shot. In September 2008, the Optech Gemini instrument flew over TEF to acquire lidar data at an averaged point density of 14.7 shots per square meter, with up to four returns per laser shot. At LSBS, the lidar data were collected in September and October of 2009. The Optech ALTM 3100EA instrument was used for this site, and achieved an averaged point density of 3.0 per square meter and up to four returns per laser shot. All these lidar surveys were carried out in clear sky conditions. There were no clouds, precipitation, atmospheric haze or blowing snow to affect the accuracy of the lidar measurements. These data were processed to simulate GEDI full-waveform data following the method of Blair and Hofton (1999) with measurement noise added following Hancock et al. (2011), summarized briefly in Section 2.2.2. It is demonstrated in a separate simulator validation paper that the GEDI simulator accurately creates full-waveform, large-footprint lidar signals from data from all ALS instruments and beam densities in these investigations (Hancock et al. 2019).

HBEF   TEF   LSBS

Cloud-free GEDI elevation

50%-cloud GEDI elevation

Cloud-free GEDI canopy height

50%-cloud GEDI canopy height

173

Fig. 2 Simulated GEDI observations of elevation and canopy height over nominal two-year period based on cloud-free and 50%-cloud cover conditions.

2.2.2 Simulated GEDI observations from ALS data

Our GEDI simulation in this study is based on an earlier system configuration. In this configuration, GEDI was comprised of three identical lasers (Coyle et al. 2015; Stysley et al. 2015), two of which were split into four beams (what we call "coverage beams"). The power of the coverage beam after splitting was about half that of the strong beam. These five beams were dithered across-track on every other line to produce 10 parallel ground tracks with approximately 600 m spacing across track and 60 m spacing along track. The GEDI across-track ground swath width (the distance from beams 1 to 10) was therefore approximately 5.4 km. The inclination of tracks relative to north, determined by the inclination of the ISS orbit (Qi and Dubayah 2016), was,

185 and still is, latitude-dependent and thus different for each site (see Fig. 1). After simulating the

186 likely number of times the 10-beam pattern of GEDI would cross each site after the full two-year

187 period, we obtained the track patterns for leaf-on orbits under cloud-free condition as shown in the

188 upper row of Fig. 1.

189 The finalized GEDI lidar system to be deployed on ISS has a different configuration. Only one

190 of the three lasers is split into two coverage beams and the other two lasers are not split. This new

191 configuration produces a total of four beams (two coverage and two full power beams) and thus

192 eight parallel ground tracks after beam dithering. The spacings of footprints across track and along

193 track are not changed, being about 600 m and 60 m respectively. The ground swath width is thus

194 approximately 4.2 km. This eight-beam pattern of GEDI generally gives about 20% less GEDI

195 footprints compared to those provided by a 10-beam pattern GEDI within our simulations here,

196 and the difference should have a small impact on our results, as discussed later in Section 5.

197 Since future local cloud conditions for each GEDI orbital pass are unknown, an estimate of

198 ~50% for the mean global cloud cover (Downs and Day 2005) was applied to obtain the track

199 patterns under cloudy condition for all sites (see lower row in Fig. 1). Specifically, the impact of

200 data losses due to cloud cover was simulated by removing complete GEDI tracks. For each track,

201 a random number (0-1) was selected and if that number was greater than the cloud over (0.5), it

202 was used. If it was less, all GEDI footprints in that track were rejected. This assumes that the cloud

203 length scale was large enough to remove a complete track, but not so large that adjacent tracks

204 were affected. Both track patterns under cloud-free and 50%-cloud conditions were then used as

205 templates for the extraction of ALS-derived waveforms to simulate GEDI observations (see Fig.

206 2).

207   In the simulation process, GEDI is modelled as a Gaussian shaped laser footprint with a width

208   (1 sigma) of 5.5 m (an effective footprint size of 22 m) a near Gaussian outgoing laser pulse shape

209   of length (full width half maximum) 15.6 ns and a range resolution of 15 cm. The expected signal

210   to noise ratio has been estimated for mean atmospheric transmission and surface reflectance and a

211   3 db loss of link margin added to make predictions more conservative. To simulate GEDI signals,

212   discrete return ALS points are taken to be representative of the vertical distribution of surfaces.

213   All ALS points within 17.4 m horizontally of the footprint center were included (corresponding to

214   an intensity of 0.06 % of the maximum). The contribution of each was weighted by the GEDI

215   footprint intensity at that point, convolved along the vertical axis by the outgoing laser pulse shape

216   and added up into an array binned to 15 cm resolution. White Gaussian noise was added to give

217   the expected signal-to-noise ratio (Davidson and Sun 1988; Hancock et al. 2011).

218   A "truth" ground elevation was identified from the high-resolution ALS data (Isenberg 2011)

219   and canopy height was calculated relative to that ground surface as the 98th percentile (RH98)

220   (Drake et al. 2002).

221   The simulated GEDI waveforms were processed to extract waveform metrics. Denoising was

222   achieved by smoothing the waveform by a Gaussian of FWHM 11ns (75% of GEDI system pulse)

223   (Hofton et al. 2000). The mean and standard deviation of the noise was calculated from the values

224   of the first 10 m of each waveform. The mean noise was subtracted and a threshold was set equal

225   to 3.5 times the standard deviation. All signal not greater than the threshold for at least three

226   consecutive waveform bins was set to zero. The ground was identified by Gaussian fitting to the

227   denoised waveforms (Hofton et al. 2000) and relative height (RH) metrics calculated. The GEDI

228   estimate of height was taken as the 98th percentile (RH98) (Drake et al. 2002).

2.2.3 TDX data

The simulated GEDI data were based on ALS data acquired pre-TDX-launch. We therefore used TDX acquisitions closest in time, to minimize temporal discrepancies. Specifically, TDX acquisitions in 2011 were used for TEF and LSBS test sites; for HBEF, both 2011 (leaf-on) and 2012 (leaf-off) acquisitions were used (Table 1). Selection of TDX data within the desired temporal windows was further refined based on their Height of Ambiguity (*HoA*) values. *HoA* can be calculated as $2\pi/\kappa_z$ (see Section 3.1 for the definition of κ_z and its use in RVoG model) and defines the maximum height retrieval allowed by a specific acquisition geometry (Kugler et al. 2015). In terms of polarization state, we only explored *HH* data because of its availability at the global scale (Krieger et al. 2007; Kugler et al. 2014). All data were acquired in bistatic mode, where one satellite was transmitting and both satellites were simultaneously receiving the returned signal, and thus had no temporal decorrelation effect (Abdullahi et al. 2016; Kugler et al. 2014; Lee and Fatoyinbo 2015).

The time difference between the ALS and TDX acquisitions was 2–3 years for HBEF, 3 years for TEF and 2 years for LSBS. The magnitude of forest change was minor over most undisturbed places within these time intervals (Dubayah et al. 2010; Smith et al. 2005; Van Doorn et al. 2011). All areas disturbed between the acquisition dates of ALS and TDX data were removed using ancillary disturbance product from Landsat images (Huang et al. 2010). No precipitation was observed on the dates of the TDX acquisitions for leaf-on HBEF, TEF and LSBS. However, a high precipitation rate was observed near the acquisition date for leaf-off HBEF (0.20 inches on that day and 0.82 inches on the day before) (NOAA), leading to a different forest water content compared to that observed for the lidar acquisition (Kugler et al., 2014), discussed later in Section 4.

252 Table 1. Summary of TDX acquisitions over the study areas.

| Study area	HBEF (temperate mixed forest)		TEF (mountainous conifer forest)	LSBS (tropical broadleaf forest)
Acq. Date	2011/10/21 (Leaf-on)	2012/01/28 (Leaf-off)	2011/12/10	2011/12/05
Eff. Bsl. (m)	121.42	85.37	103.59	89.43
HoA (m)	-47.43	-68.12	-64.47	67.79
Rg. Res. (m)	2.99	2.99	2.71	1.93
Az. Res. (m)	3.30	3.30	3.30	6.60
Pol.	HH	HH	HH	HH, VV
Inc. Ang. (°)	36.2	36.1	40.7	37.7

253

254 *Acq. Date – Acquisition Date (Year/Month/Day); Eff. Bsl. – Effective Baseline; HoA – Height

255 of ambiguity; Rg. Res. – Range Resolution; Az. Res. – Azimuth Resolution; Pol. – Polarization;

256 Inc. Ang. – Incident Angle.

257 **3   Single-polarization RVoG inversion and combination with GEDI data**

258 *3.1   RVoG model and height inversion from single-pol InSAR data*

259
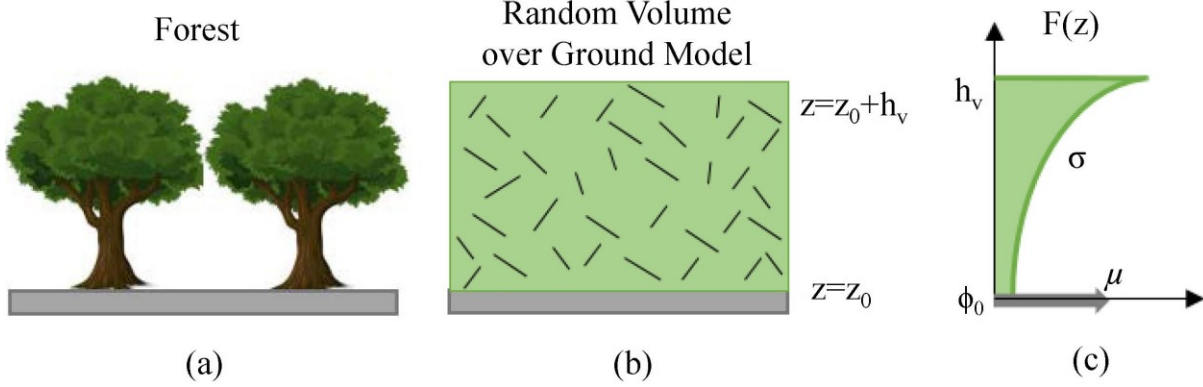
Fig. 3 The basis of the RVOG model. Forest structure in (a) is modeled using the two-layer scattering model in (b) with ground elevation z_0 and volume height (h_V). Scatterers are randomly distributed and oriented inside the forest volume (Cloude and Papathanassiou 2003). $F(z)$, radar reflectivity of forest scatterers at different height z, decays as a function of extinction coefficient (σ) as shown in (c). The term φ_0 denotes the ground phase ($e^{i\varphi_0} = e^{i\kappa_z z_0}$) and μ is the ground-to-volume amplitude ratio (Cloude and Papathanassiou 2003).

Random Volume over Ground (RVoG) model is a widely used two-layer scattering model (see Fig. 3) that enables the inversion of physical forest parameters from InSAR coherences. Based on the RVoG model, the complex interferometric coherence $\tilde{\gamma}$ at a polarization ($\vec{\omega}$), after compensating system and geometry induced decorrelation effects (Kugler et al. 2015), can be simply represented by equation (1),

$$\tilde{\gamma} \qquad \overline{\qquad \qquad \atop 1+\mu(\vec{\omega})} \tag{1}$$

where φ_0 is the phase corresponding to the ground elevation z_0; and $\mu(\vec{\omega})$ denotes the (polarization-dependent) ratio of powers echoed from ground and forest volume (Hajnsek et al. 2009; Kugler et al. 2014; Papathanassiou and Cloude 2001) (Fig. 3). Since this study only works with *HH* TDX data ($\vec{\omega} = HH$), $\tilde{\gamma}$ will be written as $\tilde{\gamma}$ and $\mu(\vec{\omega})$ as μ hereafter. $\tilde{\gamma}$ represents

277   volume coherence and can be described by a Fourier relationship of the vertical profile of the radar

278   reflectivity $F(z)$ and the volume height h_V,

279
$$\tilde{\gamma}_v = \frac{\int_0^{h_V} F(z')\, e^{i\kappa_z z'}\, dz'}{\int_0^{h_V} F(z')\, dz'} \tag{2}$$

280   where κ_z is the effective vertical wavenumber. Therefore, when the ground-to-volume amplitude

281   ratio (μ) was zero, the correlation coefficient $\left| \tilde{\gamma} \right| = \left| \tilde{\gamma}_v \right|$. The estimation of h_V requires the

282   parameterization of $F(z)$. A widely and successfully employed approach is to assume that the

283   distribution of scatterers decreases exponentially from the volume top downward, i.e.,

284    $F(z) = e^{\frac{2\sigma}{\cos\theta} z}$ where θ describes the incidence angle and σ, the mean extinction coefficient,

285   represents the attenuation rate of the wave within the volume (see Fig. 3) (Cloude and

286   Papathanassiou 2003; Papathanassiou and Cloude 2001).

287   Single-pol InSAR inversion is an underdetermined problem, meaning that the number of

288   observables from the interferometric coherence is smaller than the number of the unknown

289   parameters. Previous studies solved this problem with two constraints: 1) using an external digital

290   terrain model (DTM) to estimate ground phase (φ_0) or using a fixed mean extinction coefficient

291   (σ) for the entire study site; and 2) assuming a zero ground-to-volume amplitude ratio ($\mu=0$) at the

292   polarization state of the acquisition. However, external DTMs are often unavailable over large

293   areas, and the accuracy of height inversion may be compromised when a fixed σ (as opposed to

294   one that varies spatially) is used (Hajnsek et al. 2009; Kugler et al. 2014). Also, ground scattering

295   may be present (i.e. $\mu\neq0$) in areas with low forest density or low vegetation water content (Kugler

296   et al. 2014). To overcome these issues, we assess the efficacy of using GEDI-derived DTM and

297   canopy heights to provide the needed prerequisite information for TDX single-pol inversion.

3.2   Combining RVoG single-pol InSAR inversion with GEDI data

299

300
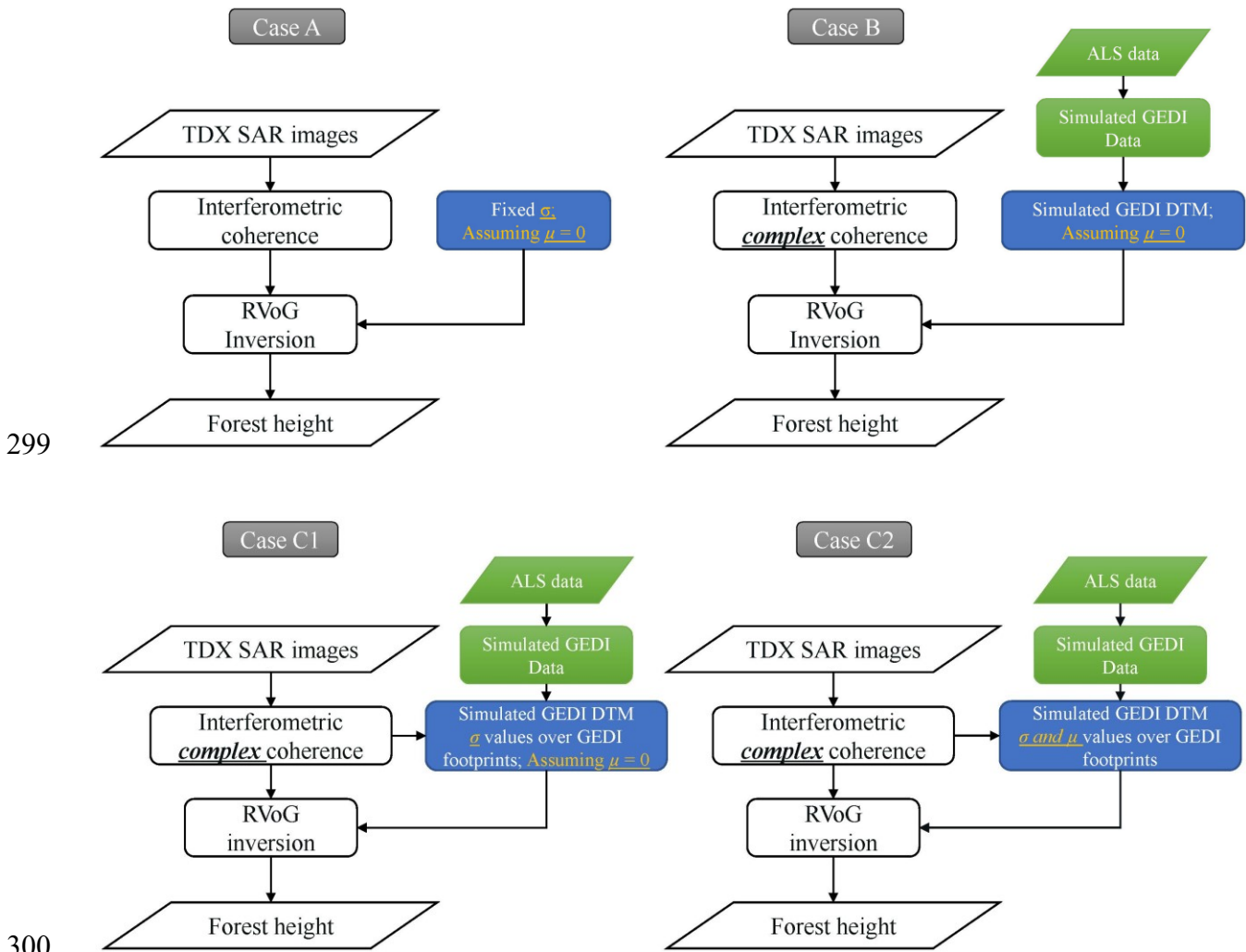
301   Fig. 4 Main procedures for the four different fusion approaches – cases A, B, C1 and C2.

302   Table 2. RVoG model parameterization for different cases performed in this study.

| Cases	Used TDX observables	Added Inputs for RVoG	RVoG parameters
A Only TDX (Baseline)	Magnitude of coherence	Assumptions for σ and μ	$\sigma = constant$; $\mu = 0$
B Using GEDI DTM	Complex coherence	Ground phase φ_0 from GEDI DTM; Assumption for μ	σ map that is purely data-driven; $\mu = 0$

17

C1 & C2 Using GEDI height and DTM	Complex coherence	C1) Ground phase φ_0 from GEDI DTM; Forest height over GEDI footprints for estimating σ; Assumption for μ	σ map interpolated from σ values along GEDI tracks; $\mu = 0$
		C2) Ground phase φ_0 from GEDI DTM; Forest height over GEDI footprints for estimating σ and μ	σ and μ maps interpolated from σ and μ values along GEDI tracks

303

304   We perform a set of three analyses (Fig. 4) where DTM and tree height variables derived from

305   simulated GEDI Lidar data were added progressively as inputs to improve the parameterization of

306   single-pol RVoG inversion, enabling an examination of the respective performance gain on height

307   estimation.

308   ***Case A – Only TDX.*** This case served as a baseline to assess what improvements in canopy

309   height accuracy, if any, would be achieved from the addition of data derived from GEDI. Here,

310   forest height was derived solely from the magnitude of TDX interferometric coherence $|\tilde{\gamma}|$ (i.e.

311   interferometric correlation coefficient) by using a constant value of extinction coefficient (σ) and

312   a zero ground-to-volume amplitude ratio ($\mu=0$) assumption (see Table 2 case A). A key step of

313   this method is to determine an appropriate σ value that in general represents forest density and

314   dielectric constant for the entire study site. For a particular acquisition with *HoA* larger than forest

315   height, a σ value higher than optimum often leads to an overestimation of h_V whereas a σ value

316   lower than optimum may result in an underestimation of h_V (see Fig. 5) (Caicoya et al. 2012;

317   Hajnsek et al. 2009). The presence of ground scattering that violates the $\mu=0$ assumption may also

318   lead to increased errors in tree height estimation (Kugler et al. 2014). Previous studies found a

319   variation of 0.3 dB/m – 1 dB/m for σ values in temperate leaf-on broadleaf forest (Kugler et al.

320   2010), 0 – 0.4 dB/m in conifer forest (Caicoya et al. 2012) and 0.1 dB – 0.9 dB/m in tropical

321   broadleaf forest (Hajnsek et al. 2009). Forest heights had been retrieved using a constant σ value

322   of 0.3 dB/m for a tropical forest and a leaf-on temperate forest (Hajnsek et al. 2009; Kugler et al.

323   2010), and a value of 0.2 dB/m for a conifer forest (Caicoya et al. 2012). In this study, we applied

324   similar σ values of 0.3 dB/m for leaf-on HBEF and LSBS, and 0.2 dB/m for TEF. The relatively

325   smaller extinction of 0.2 dB/m was applied for leaf-off HBEF as better penetration capability of

326   TDX was usually observed for leaf-off deciduous forest due to the relatively lower canopy cover

327   and forest density (Abdullahi et al. 2016; Olesk et al. 2015).
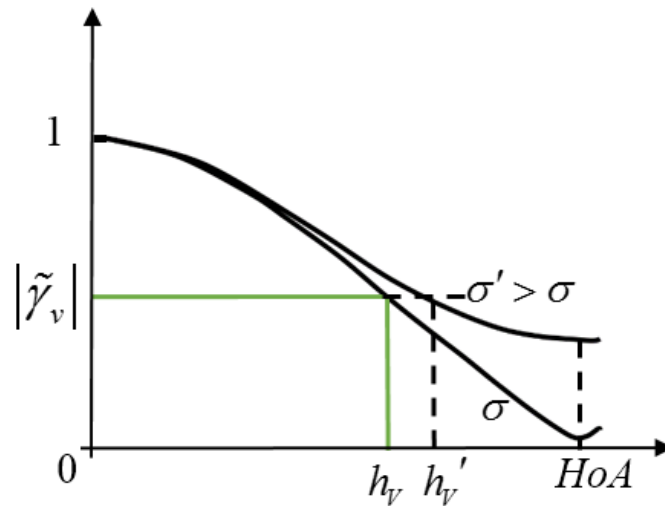
328

329   Fig. 5 An increase of h_V up to *HoA* corresponds to the decrease of $|\tilde{\gamma}_v|$ for a fixed σ. For the same

330    $|\tilde{\gamma}_v|$ value, a higher σ' value derived a larger forest height h_V'.

331
332   ***Case B – Using a simulated GEDI DTM.*** This case was designed to examine the impact of

333   adding a GEDI-derived DTM on the TDX RVoG inversion. The DTM was created at 30 m

334   resolution using simulated GEDI elevation data and a widely used spherical semivariogram model

335   for the kriging-interpolation method to characterize the spatial autocorrelation of geolocated

336   measurements (Goovaerts 2000; Maselli and Chiesi 2006). Ground phase (φ_0) was estimated from

337   this DTM and subsequently used to derive forest scattering phase (φ); φ equals TDX interferogram

338   ($\varphi_{\_interf}$) subtracted by flat-earth-phase ($\varphi_{\_flat}$) and ground phase φ_0; both $\varphi_{\_interf}$ and $\varphi_{\_flat}$ can be

339   calculated from TDX acquisitions. The scattering phase (φ), combined with the interferometric

340   correlation coefficient ($|\tilde{\gamma}|$), allowed the establishment of a balanced single-pol RVoG inversion

341   after using the $\mu=0$ assumption to derive h_V and σ (see Table 2 case B). Compared to the fixed σ

342   value employed in case A, data-driven σ values may reflect better the variation of forest

343   environment, such as volume density and vegetation water content, and thus enhance the h_V

344   inversion. However, because the accuracy of scattering phase (φ) estimation is sensitive to the

345   accuracy of the GEDI-derived DTM that derived φ_0 (Qi and Dubayah 2016), efficacy of this

346   method is impacted by the available lidar shot density and the local topography variation, i.e. if

347   the DTM is created from sparse data and the topography has large variation at local scales, the

348   kriged DTM may not capture this variation accurately.

349   ***Case C1 and C2 – Using a simulated GEDI DTM and GEDI canopy heights.*** In these two

350   cases, we assessed the effect of using both DTM and canopy height from simulated GEDI data on

351   RVoG height inversion. The auxiliary information from lidar enabled the determination of two

352   RVoG parameters over GEDI tracks (σ and μ), to constrain the inversion. To quantify the

353   performance gain, we designed cases C1 and C2 to parameterize these variables progressively with

354   the added lidar inputs. First, for case C1, we calculated only σ values (kriging was then used to

355   estimate σ for the entire study area), assuming $\mu=0$ as in previous cases, and tested the

356   improvement of h_V estimation (see Table 2 case C1). By constraining σ with the additional input

357   of simulated GEDI canopy height, case C1 was expected to be less sensitive to errors of DTM

358   estimation than case B. Second, to further evaluate the effect of using GEDI-based RVoG

359   parameterization, we calculated both σ and μ values and applied their interpolated maps (based on

360   kriging) to derive h_V (see Table 2 case C2). Over areas where ground scattering is present, we

361   hypothesize that case C2 can reflect better forest structure variation and thus should outperform

362 case C1, which assumed no scattering from ground (i.e. $\mu=0$). For all cases, the derived forest

363 height maps were resampled at 30 m resolution and subsequently averaged to 90 m (using a 3×3

364 window) to compare against reference lidar canopy heights. Note that for cases B, C1 and C2,

365 results along the simulated GEDI tracks were excluded in the averaging and comparison process,

366 considering that the simulated GEDI elevation and/or canopy height data were used to constrain

367 the RVoG model parameterization.

368 **4   Results**

369 *4.1   Case A – Only TDX*

370 Following the method described in Section 3.2 (Case A), we derived forest heights directly

371 from TDX correlation coefficient ($|\tilde{\gamma}|$) using fixed σ values of 0.3 dB/m (for leaf-off, 0.2 dB/m

372 was used for leaf-on condition), 0.2 dB/m, and 0.3 dB/m respectively for HBEF, TEF, and LSBS

373 (Fig. 6). As mentioned earlier, for a particular acquisition with *HoA* larger than forest height, the

374 use of a σ value that is too high may result in an overestimation of h_V, and vice versa. Biases of 6.4

375 m (leaf-on)/11.9 m (leaf-off), 4.2 m and 4.9 m were respectively found for HBEF, TEF and LSBS.

376 These results indicated that optimum σ values may be smaller than those were used here. The

377 particularly large bias at HBEF during leaf-off season may also be related to the violation of the

378 $\mu=0$ assumption as there are areas of low canopy cover that could lead to ground scattering, and a

379 possibly high level of forest water content due to the high precipitation rate near the acquisition

380 date.

21
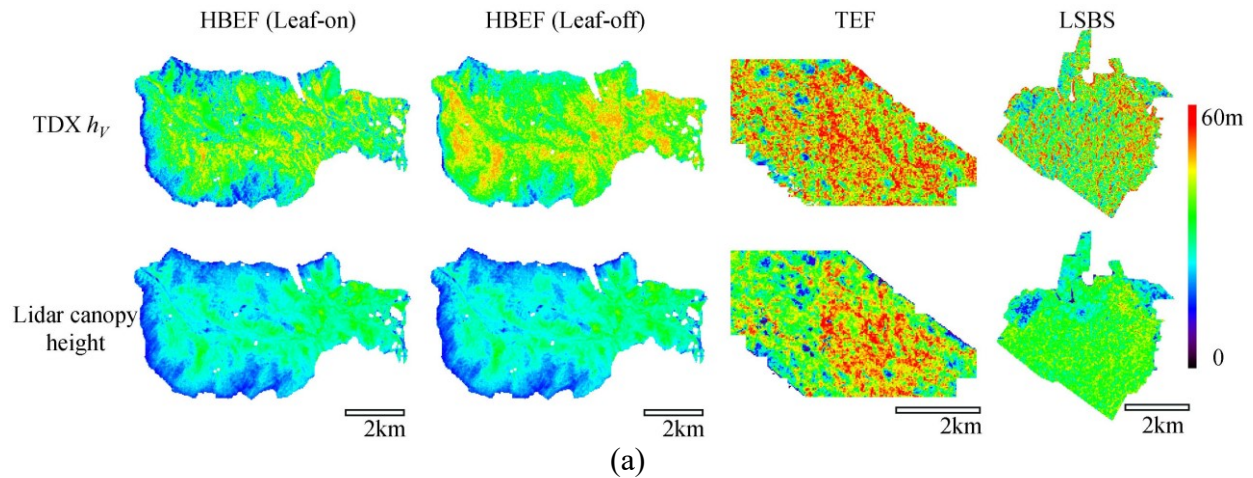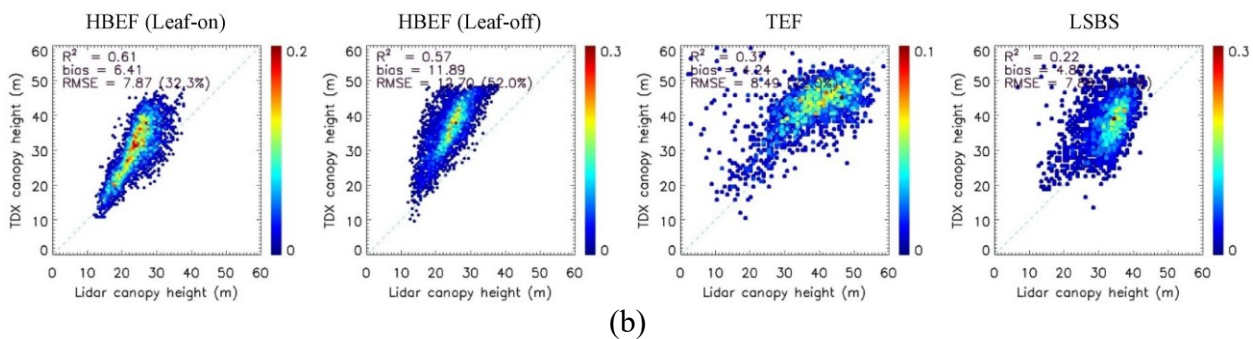
Fig. 6 (Case A) (a) Forest heights derived using fixed extinction (σ) values of 0.3 dB/m (for leaf-off, 0.2 dB/m was used for leaf-on condition), 0.2 dB/m, and 0.3 dB/m respectively for HBEF, TEF, and LSBS. (b) Comparisons of the derived heights and reference lidar heights at 90 m resolution.

The coefficient of determination observed between the derived heights and reference heights at HBEF was good (r^2 = 0.61 for leaf-on and 0.57 for leaf-off conditions), indicating an overall homogeneous forest structure (because only one σ was given) and good explanatory power of TDX $|\tilde{\gamma}|$ at this site. In contrast, lower coefficient of determination were found at TEF (r^2=0.37) and LSBS (r^2=0.22), probably resulting from the lower explanatory power of the used TDX coherences, given that TDX signal is expected to have less penetration capability over areas with taller trees and higher forest density. In addition, these sites have a somewhat heterogeneous forest

399   structure, and therefore an expectation that σ may have a larger spatial variation and thus is less

400   suitable for using the fixed value assumption.

4.2   Case B – Using simulated GEDI DTM

402   We estimated a scattering phase (φ) map for each site using the external DTM derived from

403   simulated GEDI elevation data. Forest height (h_V) as well as extinction (σ) were then derived from

404   the RVoG model using φ and correlation coefficient ($|\tilde{\gamma}|$) as inputs. Moderate agreement was

405   found between the heights derived using cloud-free GEDI vs. lidar canopy heights, with r^2 of 0.39

406   (leaf-on) / 0.32 (leaf-off), 0.53 and 0.38 respectively at HBEF, TEF and LSBS (see Fig. 7 and

407   Table 3). Biases were reduced to 2.0 m (leaf-on) / 2.4 m (leaf-off) for HBEF, 1.7 m for TEF and

408   4.2 m for LSBS. Relatively lower agreement was found when using GEDI under 50% cloud cover,

409   with r^2 of 0.17 (leaf-on) / 0.12 (leaf-off), 0.42 and 0.32, and biases of 2.6 m (leaf-on) / 2.4 m (leaf-

410   off) for HBEF, 2.4 m for TEF and 3.8 m for LSBS. As mentioned earlier, σ represents the

411   attenuation rate of the microwave signal inside the forest volume and reflects the variation of forest

412   scatterer density and dielectric constant. Therefore, compared to case A which used a fixed σ, case

413   B provided improved height estimates by exploiting a spatially varying σ, providing a better fit to

414   the environmental condition at the time of acquisition.

415
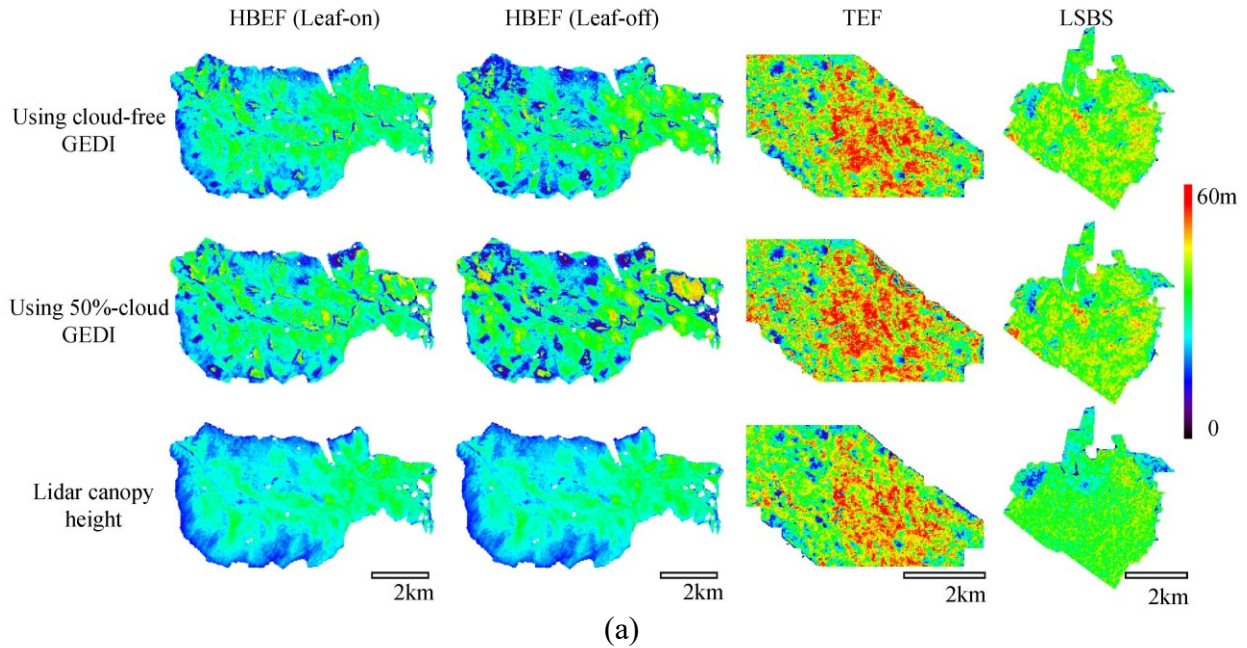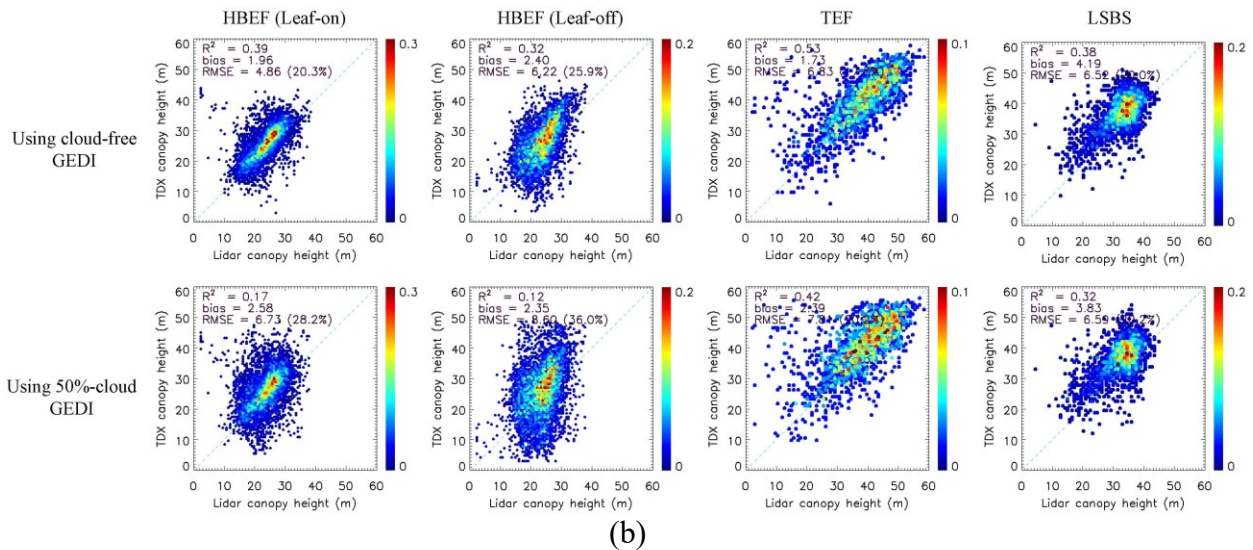
Fig. 7 (Case B) (a) Forest heights derived from complex TDX coherence using simulated GEDI

DTM, based on cloud-free and 50%-cloud cover conditions. (b) Comparisons of the derived

heights and reference lidar heights at 90 m resolution.

Table 3. Validation results of RVoG heights from all cases at 90 m resolution.

24

Cases	Validation Parameters	HBEF				TEF		LSBS	
		Leaf-on		Leaf-off		-		-	
		Cloud-free	50%-cloud	Cloud-free	50%-cloud	Cloud-free	50%-cloud	Cloud-free	50%-cloud
Case A	r^2	0.61		0.57		0.37		0.22	
	Bias (m)	6.41		11.89		4.24		4.89	
	RMSE (m)	7.87		12.70		8.49		7.88	
	RMSE (%)	32.3		52.0		22.0		23.9	
Case B	r^2	0.39	0.17	0.32	0.12	0.53	0.42	0.38	0.32
	Bias (m)	1.96	2.58	2.40	2.35	1.73	2.39	4.19	3.83
	RMSE (m)	4.86	6.73	6.22	8.60	6.83	7.81	6.52	6.59
	RMSE (%)	20.3	28.2	25.9	36.0	17.7	20.2	20.0	20.2
Case C1	r^2	0.51	0.26	0.50	0.21	0.60	0.49	0.43	0.38
	Bias (m)	0.60	0.90	-0.70	-0.80	-1.01	-0.81	0.84	0.28
	RMSE (m)	3.95	5.56	4.21	6.60	6.03	6.65	4.66	5.03
	RMSE (%)	16.5	23.2	17.5	27.5	15.6	17.1	14.2	15.4
Case C2	r^2	0.70	0.37	0.68	0.31	0.56	0.42	0.44	0.39
	Bias (m)	-0.42	0.12	0.17	0.94	-0.69	-0.51	0.55	0.19
	RMSE (m)	2.63	4.03	2.66	4.98	6.12	7.14	4.30	4.64
	RMSE (%)	10.9	16.7	11.1	20.7	15.9	18.5	13.1	14.2

428
429

430   *4.3   Cases C1 and C2 – Using simulated GEDI DTM and canopy heights*

431   As described in 3.2, simulated GEDI observations of DTM and canopy height were combined

432   to assist the parameterization of RVoG based on two approaches, either refining σ alone (case C1)

433   or σ and μ combined (case C2).

434   For case C1, simulated GEDI-derived extinction coefficient (σ) values were employed.

435   Compared to case B which just used the external GEDI-derived DTM, the constraining of σ from

436   additional GEDI height information enhanced the single-pol inversion as expected. When using

437   cloud-free GEDI observations, improved correlation between estimated height and lidar reference

438   was obtained, with r^2 of 0.51 (leaf-on) / 0.50 (leaf-off), 0.60 and 0.43 respectively at HBEF, TEF

439   and LSBS. Biases were reduced to 0.6 m (leaf-on) / -0.7 m (leaf-off) for HBEF, -1.0 m for TEF

440   and 0.8 m for LSBS. The RMSEs were 4.0 m (relative error of 17% for leaf-on) / 4.2 m (18% for

441   leaf-off), 6.0 m (16%), and 4.7 m (14%) respectively (see Fig. 8, Table 3). When using GEDI

442   under 50% cloud cover, height estimates were also improved compared to case B under the same

443   GEDI coverage, with r^2 of 0.26 (leaf-on) / 0.21 (leaf-off), 0.49 and 0.38 respectively at HBEF,

444   TEF and LSBS. Biases of 0.9 m (leaf-on) / -0.8 m (leaf-off), -0.8 m and 0.3 m, and RMSEs of 5.6

445   m (relative error of 23% for leaf-on) / 6.6 m (28% for leaf-off), 6.7 m (17%) and 5.0 m (15%) were

446   found for the three sites (see Fig. 8, Table 3). These results showed that by constraining σ

447   estimation alone using local tree height information from GEDI, single-pol RVoG height inversion

448   is significantly improved under a μ=0 assumption.
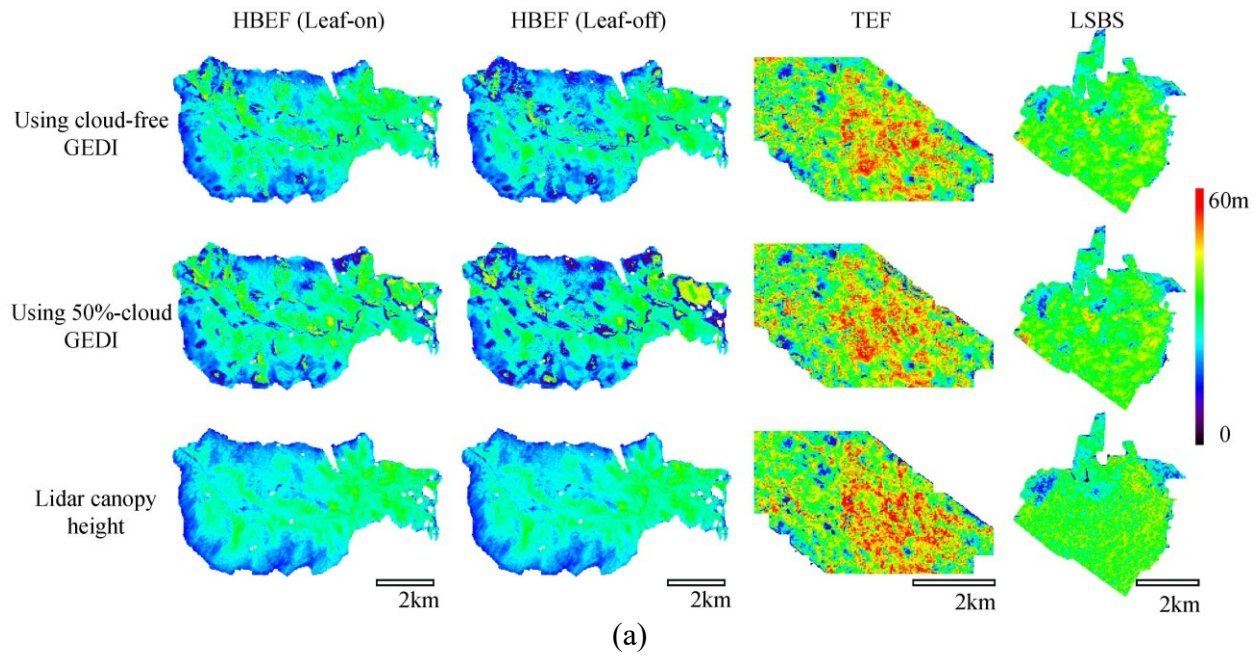
449
450
451

(a)

452
453

(b)

454
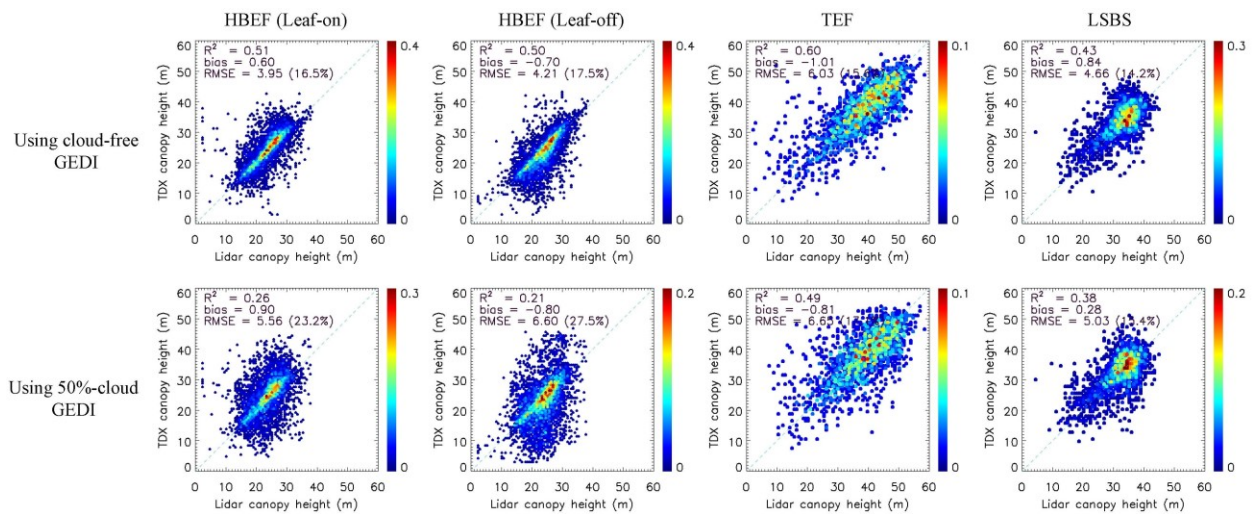
455 Fig. 8 (Case C1) (a) Forest heights derived from complex TDX coherence using DTM and canopy

456 height derived from simulated GEDI observations, respectively based on cloud-free and 50%-

457 cloud conditions, to constrain σ. (b) Comparisons of the derived heights and reference lidar heights

458 at 90 m resolution.
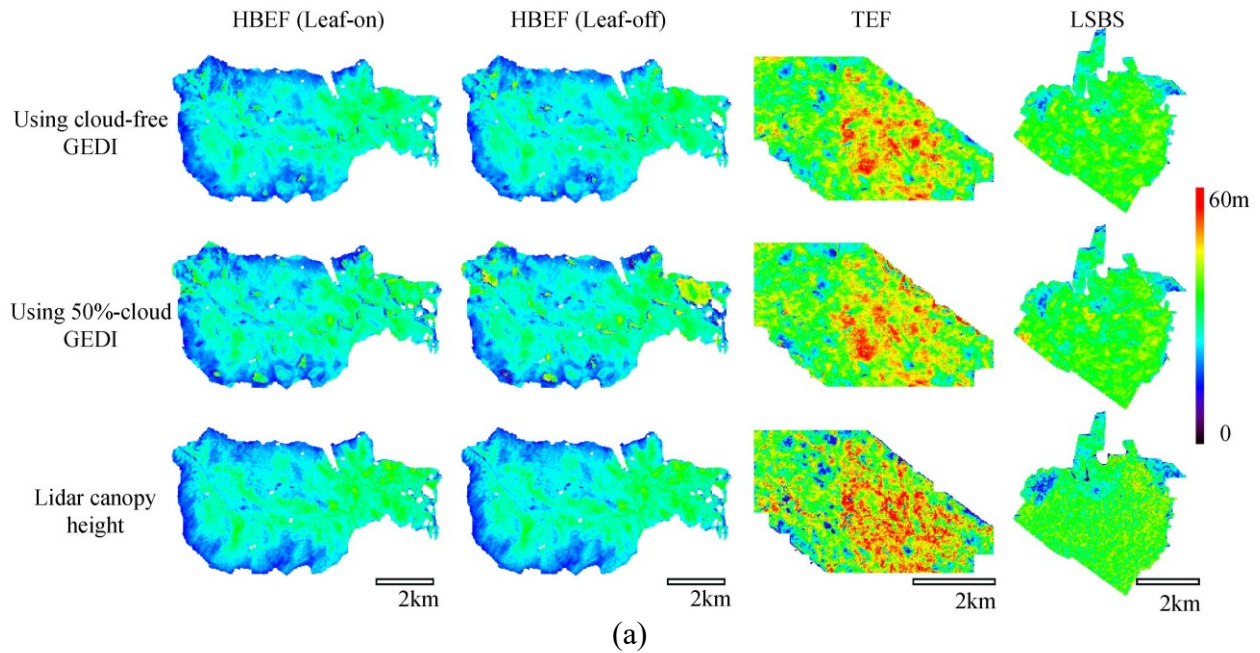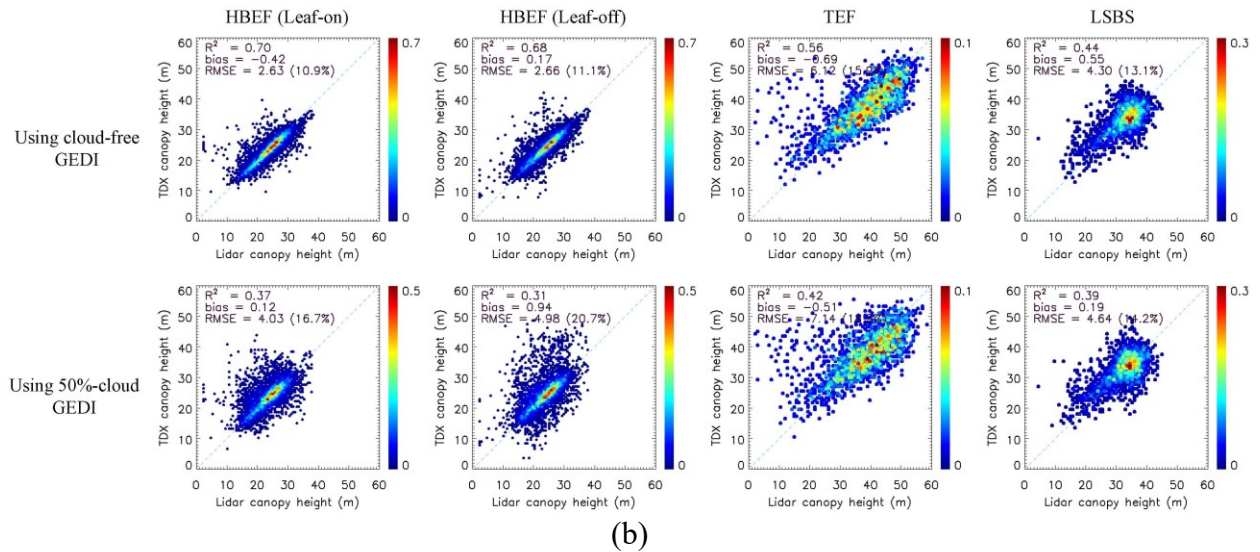
459
460

Fig. 9 (Case C2) (a) Forest heights derived from complex TDX coherence using DTM and canopy height derived from simulated GEDI observations, respectively based on cloud-free and 50%-cloud cover conditions, to constrain σ and μ. (b) Comparisons of the derived heights and reference lidar heights at 90 m resolution.

The second method (case C2) was the only approach that derived both extinction coefficient (σ) and ground-to-volume amplitude ratio (μ) values to improve the height inversion. This was

28

473   made possible by adding both simulated GEDI canopy height and GEDI-derived DTM as inputs.

474   These σ and μ values were interpolated and used jointly to calculate forest height from the complex

475   coherence ($\tilde{\gamma}$). The estimated heights were improved at HBEF relative to all other cases. When

476   using cloud-free GEDI data, we found r^2 values of 0.70 (leaf-on) / 0.68 (leaf-off), biases of -0.4 m

477   (leaf-on) / 0.2 m (leaf-off) and RMSEs of 2.6 m (11% for leaf-on)/ 2.7 m (11% for leaf-off). When

478   using 50% cloud-cover GEDI data, r^2 of 0.37 (leaf-on) / 0.31 (leaf-off), biases of 0.1 m (leaf-on) /

479   0.9 m (leaf-off), and RMSEs of 4.0 m (17% for leaf-on)/ 5.0 m (21% for leaf-off) were observed.

480   For each specific case (from A to C2), leaf-on TDX-derived heights had stronger agreement with

481   reference lidar heights than leaf-off TDX-heights. Somewhat paradoxically, greater improvements

482   were observed from case A to case C2 using leaf-off data at HBEF. This is mainly because leaf-

483   off forests have relatively lower volume scattering and higher ground scattering, and are more

484   likely to violate the $\mu=0$ assumption; therefore, the RVoG model using leaf-off data had greater

485   reliance on GEDI inputs (particularly canopy height) for constraining the σ and μ parameters to

486   accurately invert forest heights.

487   At TEF and LSBS, case C2 derived heights with r^2 values of 0.44–0.56 (cloud-free)/0.39–0.42

488   (50%-cloud), biases of -0.7 to 0.6 m (cloud-free)/-0.5 to 0.2 m (50%-cloud), and RMSEs of 4.3–

489   6.1 m (13%–16%, cloud-free)/4.6–7.1 m (14%-19%, 50%-cloud). The overall improvements from

490   case C1 to case C2 were not seen (at TEF) or marginal (at LSBS). This suggests a lower utility of

491   constraining the μ values in improving height estimation over areas where taller trees, higher

492   canopy cover or heterogeneous forest structure prevail (Fig. 9 and Fig. 10; Table 3).

5 Discussion

There is the potential to combine the relatively sparse, footprint level estimates of GEDI with wall-to-wall SAR measurements from TDX to provide continuous estimates of canopy height at much finer spatial resolution than what can be obtained by GEDI alone. Indeed, as currently planned, GEDI will grid its height observations to a required resolution of 1000 m. Our work presented here provides a realistic pathway towards the goal of improved height mapping at these finer resolutions.

Our study explored the efficacy of using simulated GEDI observations in improving TDX estimate of canopy heights. The utility of two GEDI-aided RVoG parameters – extinction coefficient (σ) and ground-to-volume amplitude ratio (μ) – for improving forest height estimation was assessed. These two parameters are related to forest height, density, canopy cover, as well as the dielectric constant of scatterers in a forest, and vary across the landscape in different forest environments. In previous studies, these were mainly derived using full-polarimetric InSAR data at longer-wavelength (such as L-band), which are currently unavailable at the global scale (Hajnsek et al. 2009; Kugler et al. 2015; Neumann et al. 2012). Our study demonstrated that these RVoG parameters can be effectively derived from single-pol TDX data by adding simulated GEDI observations of terrain elevation and canopy height as model inputs, and can be applied to improve forest height estimation over a wide range of forest types and terrain conditions.

In general, height estimates improved as more information was used from GEDI to parameterize the RVoG model (Fig. 10 and Table 3). Our results also demonstrated that height estimation using TDX data acquired in leaf-off conditions could be significantly improved through inclusion of GEDI data, opening up the possibility of using a much broader range of TDX acquistions in

515   temperate deciduous forests. We did not, however, evaluate the impact of using leaf-off GEDI

516   data, which is the focus of a future study.
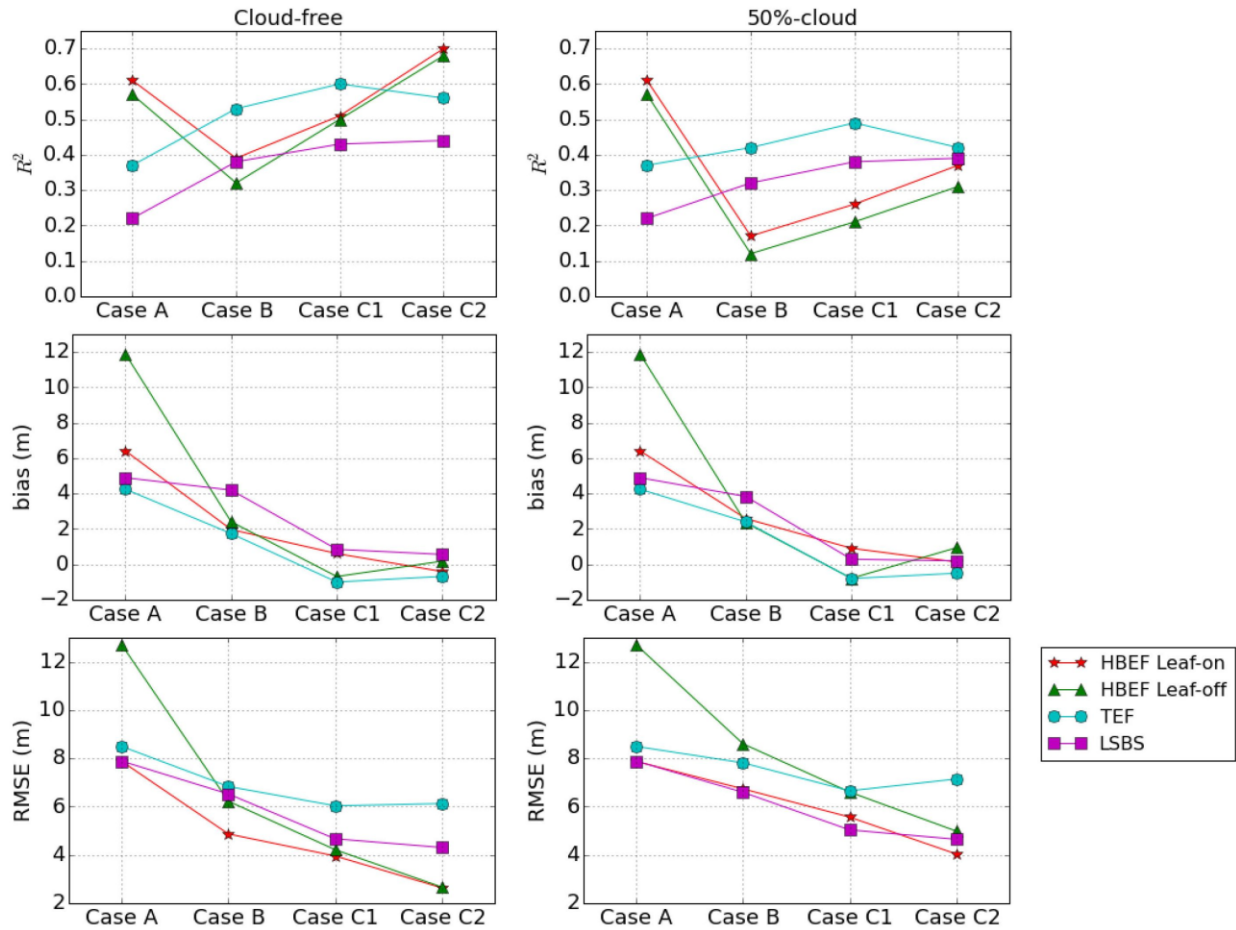
517

518   Fig. 10 Different model performance corresponding to the four different cases over HBEF, TEF

519   and LSBS under both cloud-free and 50%-cloud cover conditions.

520   The fidelity of the GEDI-derived DTM had a significant impact on the efficacy of GEDI/TDX

521   fusion. A key step to providing more accurate height products may be to enhance the GEDI DTM

522   (below canopy topography) (Lee et al. 2018) using, for example, DEM (surface elevation) products

523   from TDX (Bräutigam et al. 2014), SRTM (Rodriguez et al. 2006), Advanced Spaceborne Thermal

524   Emission and Reflection Radiometer (ASTER) (Abrams et al. 2010), or data from future missions

525   such as ICESat-2 (Abdalati et al. 2010) and NASA-ISRO Synthetic Aperture Radar (NISAR)

526   (Hoffman et al. 2016). In particular, the combination of the transect sampling lidar observations

527   from ICESat-2 and GEDI, when combined with continuous, but less accuracte surface elevation

528   meausrements from other missions (Lee et al. 2018), within an improved spatial

529   interpolation/kriging framework is a promising avenue for future research.

530   Related to this, is the fact that GEDI is limited by cloud-cover and the vagaries of the ISS

531   precessing orbit, which may limit the number of observations available for a given region (and

532   thus lead to an inaccurate DTM, for example, in those areas). When there are insufficient GEDI

533   observations for a given study site, parameters derived over limited GEDI footprints may fail to

534   cover the whole spectrum of forest structure and topographic conditions and may smooth through

535   spatial discontinuities in forest structure (see results in case C2 at TEF and LSBS). GEDI tries to

536   overcome some of this issue by pointing to acquire a more uniform track coverage. Since σ and μ

537   are related to forest structural characteristics, an alternative approach may be to input σ and μ

538   derived from the same TDX acquisition or those with similar geometries (particularly baselines)

539   over similar forest types and environmental conditions that have sufficient lidar coverage. This

540   can be done using segmentation and clustering algorithms to group segments with similar expected

541   σ and μ values, based on TDX coherence and other continuous fields (e.g. canopy cover maps from

542   Landsat) (Clewley et al. 2014). Such fusion approaches are being developed as part of a

543   collaboration between the German Aerospace Center (DLR) and the GEDI mission.

544   Extrapolation of our results to real data derived from GEDI should be done carefully. Our

545   simulated GEDI data is based on using ALS data, along with the expected ISS track patterns from

546   an earlier 10-beam pattern configuration under cloud-free and 50%-cloud cover conditions within

547 an end-end simulator (Hancock et al. 2019). While the simulator has been validated, the on-orbit

548 data from the GEDI instrument may differ from our simulations.

549 The change to an eight-beam configuration overall provides about 20% less footprints

550 compared to those from a 10-beam pattern GEDI. However, impact from such change should not

551 be large on our height estimates. In our case C2 particularly, RMSEs increased from the range of

552 2.6 – 6.2 m (10.9% - 15.9%) to a range of 4.0 – 7.1 m (14.2% - 20.7%) across the three study sites

553 after 50% tracks were removed from the cloud-free track pattern. We would thus expect a smaller

554 impact when 20% tracks (under cloud-free condition) are removed, i.e. results should be better

555 than the cloudy case, where 50% of the tracks are removed, but not as good as assuming we have

556 10 beams. For example, after using 80% tracks (to simulate the cloud-free condition from eight-

557 beam pattern GEDI) at HBEF, we observed an increased RMSE for Case C2 from 2.6 m (10.9%)

558 to 3.1 m (13.0%).

559 Note that our simulation regarding beam patterns and clouds in some ways is too conservative.

560 Cloud length scales are such that it's unlikely entire tracks will be eliminated by clouds. Rather,

561 some lidar shots may be obtained through gaps, and so our approach removes more shots than

562 likely happen. That said, the default approach GEDI is implementing is to not use any leaf-off

563 data, and to only use the coverage beams for canopy cover that is less than 70%. In our simulation

564 for HBEF we simply assumed we could use all the leaf-off data, but presented results separately

565 to provide an estimate of how well one could improve height estimates and resolution, via fusion

566 with TDX, if such data are used. Interestingly, because the current configuration now has two

567 strong beams and one coverage vs. one strong and two coverage, more GEDI footprints should be

568 usable under high canopy cover during daytime conditions, which mitigates some of the loss that

569 occurs by going from 10 to 8 tracks.

570   Another source of potential error is geolocation uncertainty. The geolocation accuracy of GEDI

571   footprints is estimated to be around 7 m at the 1-sigma level. This geolocation uncertainty was not

572   modeled in our experiments. Such error may lead to a less-accurate DTM generation for scattering

573   phase (φ) estimation over sloping surfaces and less-representative RVoG parameters of σ (and μ)

574   over heterogeneous forest structure, and thereby lower the inversion accuracy. Minimizing

575   geolocation uncertainty for GEDI has been a priority during mission development precisely so we

576   may preserve our ability to do fusion at fine spatial scales with other data.

577   One major application of height estimates (and the main driver behind the GEDI mission) is

578   forest AGB estimation. Previous studies have identified a height accuracy requirement of about 1

579   m to 2 m at 100 m to 1000 m resolution (with finer resolution more favorable) for effective biomass

580   estimates (Hall et al. 2011; Hurtt et al. 2010; Qi and Dubayah 2016). Our fusion results at 90 m do

581   not quite meet that requirement. However, one of the most important results is that fusion greatly

582   reduces bias. This is key because if bias can be kept low, the fused heights can be aggregated to a

583   coarser resolution until the desired height accuracies are achieved. For example, starting from the

584   30 m resolution at which the GEDI/TDX fusion was conducted, our height products from case C2

585   agreed with reference lidar heights (for the purpose of cross validation, heights over simulated

586   GEDI tracks were excluded from comparison; same for the 200 m resolution) at RMSEs of (leaf-

587   on / leaf-off) 3.0 m / 3.3 m at HBEF, 7.8 m at TEF and 5.8 m at LSBS under cloud-free conditions.

588   After averaging up to 200 m, RMSEs were improved to 2.0 m / 2.1 m at HBEF, 3.8 m at TEF and

589   3.4 m at LSBS under cloud-free conditions. These results demonstrated that keeping biases low

590   enables aggregation to scales that are still relatively fine, and which now approach accuracy

591   requirements. In turn, these observations can then potentially be used to drive models that estimate

34

592   biomass at scales considerably below 1 km and with accuracies presumably better than what TDX

593   can achieve by itself, as will be explored in subsequent research.

594   **6   Conclusions**

595   We have investigated the fusion of simulated Global Ecosystem Dynamics Investigation

596   (GEDI) lidar data with actual TanDEM-X (TDX) InSAR data to improve forest structure mapping

597   over three contrasting forest types covering a wide range of heights, canopy cover and topography.

598   Our results showed that forest height retrievals from TDX single-polarization InSAR acquisitions

599   based on the widely Random Volume over Ground (RVoG) were significantly improved using

600   GEDI observations of bare-ground topography and canopy top height as inputs to constrain the

601   model parameterization. Improving TDX height estimates with the aid of GEDI measurements is

602   a meaningful step towards deriving blended height products from the two missions with better

603   accuracy and coverage than using either data source alone. These height products, if sufficiently

604   accurate, should improve the potential use of these data for applications such as biomass modeling

605   and biodiversity.

612   Dr. Chengquan Huang, Dr. Feng Zhao and Dr. Min Feng for providing the forest disturbance data

613   products.

614   **References**

615   Abdalati, W., Zwally, H.J., Bindschadler, R., Csatho, B., Farrell, S.L., Fricker, H.A., Harding,
616   D., Kwok, R., Lefsky, M., Markus, T., Marshak, A., Neumann, T., Palm, S., Schutz, B., Smith,
617   B., Spinhirne, J., & Webb, C. (2010). The ICESat-2 laser altimetry mission. *Proceedings of the*
618   *IEEE, 98*, 735-751

619   Abdullahi, S., Kugler, F., & Pretzsch, H. (2016). Prediction of stem volume in complex
620   temperate forest stands using TanDEM-X SAR data. *Remote Sensing of Environment, 174*, 197-
621   211

622   Abrams, M., Bailey, B., Tsu, H., & Hato, M. (2010). The aster global dem. *Photogrammetric*
623   *Engineering and Remote Sensing, 76*, 344-348

624   Askne, J.I.H., Fransson, J.E.S., Santoro, M., Soja, M.J., & Ulander, L.M.H. (2013). Model-based
625   biomass estimation of a hemi-boreal forest from multitemporal TanDEM-X acquisitions. *Remote*
626   *Sensing, 5*, 5574-5597

627   Baccini, A.G.S.J., Goetz, S.J., Walker, W.S., Laporte, N.T., Sun, M., Sulla-Menashe, D.,
628   Hackler, J., Beck, P.S.A., Dubayah, R., Friedl, M.A., Samanta, S., & Houghton, R.A. (2012).
629   Estimated carbon dioxide emissions from tropical deforestation improved by carbon-density
630   maps. *Nature Climate Change, 2*, 182-185

631   Bergen, K.M., Goetz, S.J., Dubayah, R.O., Henebry, G.M., Hunsaker, C.T., Imhoff, M.L.,
632   Nelson, R.F., Parker, G.G., & Radeloff, V.C. (2009). Remote sensing of vegetation 3-D structure
633   for biodiversity and habitat: Review and implications for lidar and radar spaceborne missions.
634   *Journal of Geophysical Research: Biogeosciences, 114*, 13

635   Blackard, J.A., Finco, M.V., Helmer, E.H., Holden, G.R., Hoppus, M.L., Jacobs, D.M., Lister,
636   A.J., Moisen, G.G., Nelson, M.D., Riemann, R., Ruefenacht, B., Salajanu, D., Weyermann, D.L.,
637   Winterberger, K.C., Brandeis, T.J., Czaplewski, R.L., McRoberts, R.E., Patterson, P.L., &
638   Tymcio, R.P. (2008). Mapping US forest biomass using nationwide forest inventory data and
639   moderate resolution information. *Remote Sensing of Environment, 112*, 1658-1677

640   Blair, J.B., & Hofton, M.A. (1999). Modeling laser altimeter return waveforms over complex
641   vegetation using high-resolution elevation data. *Geophysical Research Letters, 26*, 2509-2512

642   Brolly, M., Simard, M., Tang, H., Dubayah, R.O., & Fisk, J.P. (2016). A Lidar-Radar
643   Framework to Assess the Impact of Vertical Forest Structure on Interferometric Coherence.
644   *IEEE Journal of Selected Topics in Applied Earth Observations and Remote Sensing, 9*, 5830-
645   5841

646 Bräutigam, B., Bachmann, M., Schulze, D., Tridon, D.B., Rizzoli, P., Martone, M., Gonzalez, C.,
647 Zink, M., & Krieger, G. (2014). TanDEM-X global DEM quality status and acquisition
648 completion. In, *Geoscience and Remote Sensing Symposium (IGARSS), 2014 IEEE International*
649 (pp. 3390-3393): IEEE

650 Caicoya, A.T., Kugler, F., Hajnsek, I., & Papathanassiou, K. (2012). Boreal forest biomass
651 classification with TanDEM-X. In, *Geoscience and Remote Sensing Symposium (IGARSS), 2012*
652 *IEEE International* (pp. 3439-3442): IEEE

653 CEOS (2014). *CEOS Strategy for Carbon Observations from Space. The Committee on Earth*
654 *Observation Satellites (CEOS) Response to the Group on Earth Observations (GEO) Carbon*
655 *Strategy.*: JAXA and I&A Corporation

656 Clark, D.B., & Kellner, J.R. (2012). Tropical forest biomass estimation and the fallacy of
657 misplaced concreteness. *Journal of Vegetation Science, 23*, 1191-1196

658 Clark, D.B., Olivas, P.C., Oberbauer, S.F., Clark, D.A., & Ryan, M.G. (2008). First direct
659 landscape-scale measurement of tropical rain forest Leaf Area Index, a key driver of global
660 primary productivity. *Ecology Letters, 11*, 163-172

661 Clark, M.L., Roberts, D.A., Ewel, J.J., & Clark, D.B. (2011). Estimation of tropical rain forest
662 aboveground biomass with small-footprint lidar and hyperspectral sensors. *Remote Sensing of*
663 *Environment, 115*, 2931-2942

664 Clewley, D., Bunting, P., Shepherd, J., Gillingham, S., Flood, N., Dymond, J., Lucas, R.,
665 Armston, J., & Moghaddam, M. (2014). A Python-Based Open Source System for Geographic
666 Object-Based Image Analysis (GEOBIA) Utilizing Raster Attribute Tables. *Remote Sensing, 6*,
667 6111-6135

668 Cloude, S.R., Chen, H., & Goodenough, D.G. (2013). Forest height estimation and validation
669 using Tandem-X polinsar. In, *IEEE International Geoscience and Remote Sensing Symposium*
670 *(IGARSS)* (pp. 1889-1892)

671 Cloude, S.R., & Papathanassiou, K.P. (2003). Three-stage inversion process for polarimetric
672 SAR interferometry. *IEE Proceedings-Radar, Sonar and Navigation, 150*, 125-134

673 Coyle, D.B., Stysley, P.R., Poulios, D., Clarke, G.B., & Kay, R.B. (2015). Laser transmitter
674 development for NASA's Global Ecosystem Dynamics Investigation (GEDI) lidar. In, *Proc.*
675 *SPIESPIE Optical Engineering+ Applications* (pp. 961208-961208): International Society for
676 Optics and Photonics

677 Davidson, F.M., & Sun, X.L. (1988). Gaussian approximation versus nearly exact performance
678 analysis of optical communication systems with PPM signaling and APD receivers. *IEEE*
679 *Transactions on Communications, 36*, 1185-1192

680 Downs, R., & Day, F. (2005). *National Geographic Almanac of Geography.*

681 Drake, J.B., Dubayah, R.O., Clark, D.B., Knox, R.G., Blair, J.B., Hofton, M.A., Chazdon, R.L.,
682 Weishampel, J.F., & Prince, S.D. (2002). Estimation of tropical forest structural characteristics
683 using large-footprint lidar. *Remote Sensing of Environment, 79*, 305-319

684 Drake, J.B., Knox, R.G., Dubayah, R.O., Clark, D.B., Condit, R., Blair, J.B., & Hofton, M.
685 (2003). Above-ground biomass estimation in closed canopy Neotropical forests using lidar
686 remote sensing: factors affecting the generality of relationships. *Global Ecology and*
687 *Biogeography, 12*, 147-159

688 Dubayah, R.O., Sheldon, S.L., Clark, D.B., Hofton, M.A., Blair, J.B., Hurtt, G.C., & Chazdon,
689 R.L. (2010). Estimation of tropical forest height and biomass dynamics using lidar remote
690 sensing at La Selva, Costa Rica. *Journal of Geophysical Research: Biogeosciences, 115*, 17

691 Duncanson, L.I., Dubayah, R.O., Cook, B.D., Rosette, J., & Parker, G. (2015a). The importance
692 of spatial detail: Assessing the utility of individual crown information and scaling approaches for
693 lidar-based biomass density estimation. *Remote Sensing of Environment, 168*, 102-112

694 Duncanson, L.I., Dubayah, R.O., & Enquist, B.J. (2015b). Assessing the general patterns of
695 forest structure: quantifying tree and forest allometric scaling relationships in the United States.
696 *Global Ecology and Biogeography, 24*, 1465-1475

697 Fatoyinbo, T.E., & Simard, M. (2013). Height and biomass of mangroves in Africa from
698 ICESat/GLAS and SRTM. *International Journal of Remote Sensing, 34*, 668-681

699 Goetz, S.J., & Dubayah, R.O. (2011). Advances in remote sensing technology and implications
700 for measuring and monitoring forest carbon stocks and change. *Carbon Management, 2*, 231-244

701 Goovaerts, P. (2000). Geostatistical approaches for incorporating elevation into the spatial
702 interpolation of rainfall. *Journal of hydrology, 228*, 113-129

703 Hajnsek, I., Kugler, F., Lee, S.K., & Papathanassiou, K.P. (2009). Tropical-forest-parameter
704 estimation by means of Pol-InSAR: The INDREX-II campaign. *IEEE Transactions on*
705 *Geoscience and Remote Sensing, 47*, 481-493

706 Hall, F.G., Bergen, K., Blair, J.B., Dubayah, R.O., Houghton, R., Hurtt, G., Kellndorfer, J.,
707 Lefsky, M., Ranson, J., Saatchi, S., Shugart, H.H., & Wickland, D. (2011). Characterizing 3D
708 vegetation structure from space: Mission requirements. *Remote Sensing of Environment, 115*,
709 2753-2775

710 Hancock, S., Armston, J., Hofton, M., Sun, X., Tang, H., Duncanson, L., Kellner, J., & Dubayah,
711 R. (2019). The GEDI simulator: A large-footprint waveform lidar simulator for calibration and
712 validation of spaceborne missions. *In review for Earth and Space Science*

713 Hancock, S., Disney, M., Muller, J.P., Lewis, P., & Foster, M. (2011). A threshold insensitive
714 method for locating the forest canopy top with waveform lidar. *Remote Sensing of Environment,*
715 *115*, 3286-3297

716 Hoffman, J.P., Shaffer, S., & Perkovic-Martin, D. (2016). NASA L-SAR instrument for the
717 NISAR (NASA-ISRO) Synthetic Aperture Radar mission. In, *Earth Observing Missions and*
718 *Sensors: Development, Implementation, and Characterization IV* (p. 988108): International
719 Society for Optics and Photonics

720 Hofton, M.A., Minster, J.B., & Blair, J.B. (2000). Decomposition of laser altimeter waveforms.
721 *IEEE Transactions on Geoscience and Remote Sensing, 38*, 1989-1996

722 Hu, T., Su, Y., Xue, B., Liu, J., Zhao, X., Fang, J., & Guo, Q.J.R.S. (2016). Mapping global
723 forest aboveground biomass with spaceborne LiDAR, optical imagery, and forest inventory data*,
724 8*, 565

725 Huang, C., Goward, S.N., Masek, J.G., Thomas, N., Zhu, Z., & Vogelmann, J.E. (2010). An
726 automated approach for reconstructing recent forest disturbance history using dense Landsat time
727 series stacks. *Remote Sensing of Environment, 114*, 183-198

728 Huang, W., Sun, G., Dubayah, R.O., Zhang, Z., & Ni, W. (2012). Mapping forest above-ground
729 biomass and its changes from LVIS waveform data. In, *IEEE International Geoscience and*
730 *Remote Sensing Symposium (IGARSS)* (pp. 6561-6564)

731 Hurtt, G.C., Fisk, J., Thomas, R.Q., Dubayah, R.O., Moorcroft, P.R., & Shugart, H.H. (2010).
732 Linking models and data on vegetation structure. *Journal of Geophysical Research:*
733 *Biogeosciences, 115*, 11

734 Isenberg, M. (2011). LAStools—Efficient Tools for LiDAR Processing. In.
735 http://www.cs.unc.edu/~isenburg/lastools/

736 Keller, M., Palace, M., & Hurtt, G. (2001). Biomass estimation in the Tapajos National Forest,
737 Brazil - Examination of sampling and allometric uncertainties. *Forest Ecology and Management,*
738 *154*, 371-382

739 Kellndorfer, J.M., Walker, W.S., LaPoint, E., Bishop, J., Cormier, T., & Fiske, G. (2012). NACP
740 aboveground biomass and carbon baseline data (NBCD 2000), U.S.A. Data set. In: Oak Ridge,
741 Tennessee, U.S.A.: ORNL DAAC

742 Krieger, G., Moreira, A., Fiedler, H., Hajnsek, I., Werner, M., Younis, M., & Zink, M. (2007).
743 TanDEM-X: A satellite formation for high-resolution SAR interferometry. *IEEE Transactions*
744 *on Geoscience and Remote Sensing, 45*, 3317-3341

745 Kugler, F., Lee, S.K., Hajnsek, I., & Papathanassiou, K.P. (2015). Forest height estimation by
746 means of Pol-InSAR data inversion: The role of the vertical wavenumber. *IEEE Transactions on*
747 *Geoscience and Remote Sensing, 53*, 5294-5311

748 Kugler, F., Sauer, S., Lee, S.K., Papathanassiou, K., & Hajnsek, I. (2010). Potential of TanDEM-
749 X for forest parameter estimation. In, *European Conference on Synthetic Aperture Radar*
750 *(EUSAR)* (pp. 1-4): VDE

751   Kugler, F., Schulze, D., Hajnsek, I., Pretzsch, H., & Papathanassiou, K.P. (2014). TanDEM-X
752   Pol-InSAR performance for forest height estimation. *IEEE Transactions on Geoscience and*
753   *Remote Sensing, 52*, 6404-6422

754   Lavalle, M., & Hensley, S. (2015). Extraction of structural and dynamic properties of forests
755   from polarimetric-interferometric SAR data affected by temporal decorrelation. *IEEE*
756   *Transactions on Geoscience and Remote Sensing, 53*, 4752-4767

757   Lee, S.K., Fatoyinbo, T., Qi, W., Hancock, S., Armston, J., & Dubayah, R.O. (2018). GEDI and
758   TanDEM-X fusion for 3D forest structure parameter retrieval. In, *International Geoscience and*
759   *Remote Sensing Symposium*. Valencia, Spain: IEEE GRSS

760   Lee, S.K., & Fatoyinbo, T.E. (2015). TanDEM-X Pol-InSAR inversion for mangrove canopy
761   height estimation. *IEEE Journal of Selected Topics in Applied Earth Observations and Remote*
762   *Sensing, 8*, 3608-3618

763   Lee, S.K., Kugler, F., Papathanassiou, K.P., & Hajnsek, I. (2013). Quantification of temporal
764   decorrelation effects at L-band for polarimetric SAR interferometry applications. *IEEE Journal*
765   *of Selected Topics in Applied Earth Observations and Remote Sensing, 6*, 1351-1367

766   Lei, Y., & Siqueira, P. (2015). An Automatic Mosaicking Algorithm for the Generation of a
767   Large-Scale Forest Height Map Using Spaceborne Repeat-Pass InSAR Correlation Magnitude.
768   *Remote Sensing, 7*, 5639

769   Maselli, F., & Chiesi, M. (2006). Evaluation of statistical methods to estimate forest volume in a
770   Mediterranean region. *IEEE Transactions on Geoscience and Remote Sensing, 44*, 2239-2250

771   Nelson, R., Margolis, H., Montesano, P., Sun, G., Cook, B., Corp, L., Andersen, H.-E., deJong,
772   B., Pellat, F.P., Fickel, T., Kauffman, J., & Prisley, S. (2017). Lidar-based estimates of
773   aboveground biomass in the continental US and Mexico using ground, airborne, and satellite
774   observations. *Remote Sensing of Environment, 188*, 127-140

775   Neumann, M., Saatchi, S.S., Ulander, L.M.H., & Fransson, J.E.S. (2012). Assessing performance
776   of L-and P-band polarimetric interferometric SAR data in estimating boreal forest above-ground
777   biomass. *IEEE Transactions on Geoscience and Remote Sensing, 50*, 714-726

778   NOAA. Daily Record of Climatological Observations. In: National Oceanic and Atmospheric
779   Administration

780   Olesk, A., Voormansik, K., Vain, A., Noorma, M., & Praks, J. (2015). Seasonal differences in
781   forest height estimation from interferometric TanDEM-X coherence data. *IEEE Journal of*
782   *Selected Topics in Applied Earth Observations and Remote Sensing, 8*, 5565-5572

783   Pan, Y., Birdsey, R.A., Fang, J., Houghton, R., Kauppi, P.E., Kurz, W.A., Phillips, O.L.,
784   Shvidenko, A., Lewis, S.L., & Canadell, J.G. (2011). A large and persistent carbon sink in the
785   world's forests. *Science, 333*, 988-993

786 Papathanassiou, K.P., & Cloude, S.R. (2001). Single-baseline polarimetric SAR interferometry.
787 *IEEE Transactions on Geoscience and Remote Sensing, 39*, 2352-2363

788 Papathanassiou, K.P., & Cloude, S.R. (2003). The effect of temporal decorrelation on the
789 inversion of forest parameters from Pol-InSAR data. In, *IEEE International Geoscience and*
790 *Remote Sensing Symposium (IGARSS)* (pp. 1429-1431)

791 Persson, H.J., Olsson, H., Soja, M.J., Ulander, L.M., & Fransson, J.E. (2017). Experiences from
792 large-scale forest mapping of Sweden using TanDEM-X data. *Remote Sensing, 9*, 1253

793 Pierce, L.E., Walker, W.S., Dobson, M.C., Hunsaker, C.T., Fites-Kaufman, J.A., & Dubayah,
794 R.O. (2002). Fusion of Optical and SAR data for forestry applications in the Sierra Nevada of
795 California. In, *IEEE International Geoscience and Remote Sensing Symposium (IGARSS)* (pp.
796 1771-1773)

797 Qi, W., & Dubayah, R.O. (2016). Combining Tandem-X InSAR and simulated GEDI lidar
798 observations for forest structure mapping. *Remote Sensing of Environment, 187*, 253-266

799 Rodriguez, E., Morris, C.S., & Belz, J.E. (2006). A global assessment of the SRTM performance.
800 *Photogrammetric Engineering & Remote Sensing, 72*, 249-260

801 Saatchi, S.S., Harris, N.L., Brown, S., Lefsky, M., Mitchard, E.T.A., Salas, W., Zutta, B.R.,
802 Buermann, W., Lewis, S.L., Hagen, S., Petrova, S., White, L., Silman, M., & Morel, A. (2011).
803 Benchmark map of forest carbon stocks in tropical regions across three continents. *Proceedings*
804 *of the National Academy of Sciences, 108*, 9899-9904

805 Schlund, M., von Poncet, F., Kuntz, S., Schmullius, C., & Hoekman, D.H. (2015). TanDEM-X
806 data for aboveground biomass retrieval in a tropical peat swamp forest. *Remote Sensing of*
807 *Environment, 158*, 255-266

808 Schwarz, P.A., Fahey, T.J., Martin, C.W., Siccama, T.G., & Bailey, A. (2001). Structure and
809 composition of three northern hardwood-conifer forests with differing disturbance histories.
810 *Forest Ecology and Management, 144*, 201-212

811 Siccama, T.G., Fahey, T.J., Johnson, C.E., Sherry, T.W., Denny, E.G., Girdler, E.B., Likens,
812 G.E., & Schwarz, P.A. (2007). Population and biomass dynamics of trees in a northern hardwood
813 forest at Hubbard Brook. *Canadian Journal of Forest Research, 37*, 737-749

814 Smith, T.F., Rizzo, D.M., & North, M. (2005). Patterns of mortality in an old-growth mixed-
815 conifer forest of the southern Sierra Nevada, California. *Forest Science, 51*, 266-275

816 Soja, M.J., Persson, H., & Ulander, L.M.H. (2014). Estimation of boreal forest biomass from
817 two-level model inversion of interferometric TanDEM-X data. In, *IEEE International*
818 *Geoscience and Remote Sensing Symposium (IGARSS)* (pp. 3398-3401)

819 Soja, M.J., & Ulander, L.M.H. (2013). Digital canopy model estimation from TanDEM-X
820 interferometry using high-resolution lidar DEM. In, *IEEE International Geoscience and Remote*
821 *Sensing Symposium (IGARSS)* (pp. 165-168)

822   Solberg, S., Astrup, R., Breidenbach, J., Nilsen, B., & Weydahl, D. (2013). Monitoring spruce
823   volume and biomass with InSAR data from TanDEM-X. *Remote Sensing of Environment, 139*,
824   60-67

825   Stysley, P.R., Coyle, D.B., Kay, R.B., Frederickson, R., Poulios, D., Cory, K., & Clarke, G.
826   (2015). Long term performance of the High Output Maximum Efficiency Resonator (HOMER)
827   laser for NASA's Global Ecosystem Dynamics Investigation (GEDI) lidar. *Optics & Laser
828   Technology, 68*, 67-72

829   Sun, G., Ranson, K.J., Guo, Z., Zhang, Z., Montesano, P., & Kimes, D. (2011). Forest biomass
830   mapping from lidar and radar synergies. *Remote Sensing of Environment, 115*, 2906-2916

831   Swatantran, A., Dubayah, R.O., Roberts, D., Hofton, M.A., & Blair, J.B. (2011). Mapping
832   biomass and stress in the Sierra Nevada using lidar and hyperspectral data fusion. *Remote
833   Sensing of Environment, 115*, 2917-2930

834   Tang, H., Brolly, M., Zhao, F., Strahler, A.H., Schaaf, C.L., Ganguly, S., Zhang, G., & Dubayah,
835   R.O. (2014). Deriving and validating Leaf Area Index (LAI) at multiple spatial scales through
836   lidar remote sensing: A case study in Sierra National Forest, CA. *Remote Sensing of
837   Environment, 143*, 131-141

838   Tang, H., Dubayah, R.O., Swatantran, A., Hofton, M., Sheldon, S., Clark, D.B., & Blair, B.
839   (2012). Retrieval of vertical LAI profiles over tropical rain forests using waveform lidar at La
840   Selva, Costa Rica. *Remote Sensing of Environment, 124*, 242-250

841   Treuhaft, R.N., Goncalves, F., dos Santos, J.R., Keller, M., Palace, M., Madsen, S.N., Sullivan,
842   F., & Graca, P. (2015). Tropical-forest biomass estimation at X-band from the spaceborne
843   TanDEM-X interferometer. *IEEE Geoscience and Remote Sensing Letters, 12*, 239-243

844   Van Doorn, N.S., Battles, J.J., Fahey, T.J., Siccama, T.G., & Schwarz, P.A. (2011). Links
845   between biomass and tree demography in a northern hardwood forest: a decade of stability and
846   change in Hubbard Brook Valley, New Hampshire. *Canadian Journal of Forest Research, 41*,
847   1369-1379

848   Whitehurst, A.S., Swatantran, A., Blair, J.B., Hofton, M.A., & Dubayah, R.O. (2013).
849   Characterization of canopy layering in forested ecosystems using full waveform lidar. *Remote
850   Sensing, 5*, 2014-2036
851